DISTANCE DETERMINATION OF RADIO-QUIET FERMI GAMMA-RAY PULSARS USING STATISTICAL METHODS

A THESIS SUBMITTED TO
THE GRADUATE SCHOOL OF NATURAL AND APPLIED SCIENCES
OF
MIDDLE EAST TECHNICAL UNIVERSITY

BY

ERTUĞRUL KARAMANLI

IN PARTIAL FULFILLMENT OF THE REQUIREMENTS
FOR
THE DEGREE OF MASTER OF SCIENCE
IN
PHYSICS

JUNE 2024

Approval of the thesis:

DISTANCE DETERMINATION OF RADIO-QUIET FERMI GAMMA-RAY PULSARS USING STATISTICAL METHODS

submitted by **ERTUĞRUL KARAMANLI** in partial fulfillment of the requirements for the degree of **Master of Science in Physics Department, Middle East Technical University** by,

Prof. Dr. Naci Emre Altun
Dean, Graduate School of **Natural and Applied Sciences** _____

Prof. Dr. Seçkin Kürkçüoğlu
Head of Department, **Physics** _____

Assoc. Prof. Dr. Sinan Kaan Yerli
Supervisor, **Physics, Middle East Technical University** _____

Assoc. Prof. Dr. Tülün Ergin Gürcan
Co-supervisor, **Physics, Michigan State University** _____

Examining Committee Members:

Prof. Dr. Altan Baykal
Physics, Middle East Technical University _____

Assoc. Prof. Dr. Sinan Kaan Yerli
Physics, Middle East Technical University _____

Prof. Dr. Osman Yılmaz
Physics, Middle East Technical University _____

Assoc. Prof. Dr. Özgür Baştürk
Astronomy and Space Sciences, Ankara University _____

Assist. Prof. Dr. Ebru Aktekin Çalışkan
Physics, Süleyman Demirel University _____

Date:29.08.2024

I hereby declare that all information in this document has been obtained and presented in accordance with academic rules and ethical conduct. I also declare that, as required by these rules and conduct, I have fully cited and referenced all material and results that are not original to this work.

Name, Surname: Ertuğrul Karamanlı

Signature :

ABSTRACT

DISTANCE DETERMINATION OF RADIO-QUIET FERMI GAMMA-RAY PULSARS USING STATISTICAL METHODS

Karamanlı, Ertuğrul
M.S., Department of Physics
Supervisor: Assoc. Prof. Dr. Sinan Kaan Yerli
Co-Supervisor: Assoc. Prof. Dr. Tülün Ergin Gürcan

June 2024, 62 pages

There are various methods to measure distances of pulsars. However, for radio-quiet pulsars, defined as gamma-ray pulsars that do not emit radio waves, none of these methods are applicable unless there is a well-known object near the pulsar. The aim of this study is to obtain the distance values of radio-silent pulsars by using statistical relationships created by pulsars with known distances.

In this study, we utilize two different methods to estimate the distances of radio-quiet pulsars. The first method employs a statistical approach, in which we perform a linear fit of six parameters in relation to gamma-ray emission efficiency. The best-fit parameters are then used to estimate the gamma-ray emission efficiency of radio-quiet pulsars, which are subsequently converted into distance values.

The second method introduces three theoretical, but experimentally consistent relations between various parameters of gamma-ray pulsars and their luminosities. These new relationships are reanalyzed through linear fitting with luminosities. The resulting fit parameters were used to determine the luminosities and distances of radio-quiet

pulsars.

Using the fit coefficients of 75 pulsars in the first method and 195 pulsars in the second method, we obtained distance predictions for 62 radio-silent pulsars. Although preliminary results indicate poor performance for the first method due to its simplicity and pure statistical nature, the distance estimations from the second method remain promising.

Keywords: Pulsars, Gamma-rays, Distance Prediction

ÖZ

RADYO-SESSİZ FERMİ GAMA IŞINI PULSARLARIN İSTATİSTİKSEL METOTLAR İLE UZAKLIK ÖLÇÜMLERİ

Karamanlı, Ertuğrul
Yüksek Lisans, Fizik Bölümü
Tez Yöneticisi: Doç. Dr. Sinan Kaan Yerli
Ortak Tez Yöneticisi: Doç. Dr. Tülün Ergin Gürcan

Haziran 2024 , 62 sayfa

Pulsarların uzaklıklarını belirlemek için çeşitli yöntemler bulunmaktadır. Ancak, radyo dalgası yaymayan gama-ışını pulsarları olarak tanımlanan radyo-sessiz pulsarlar için, pulsarın yakınında iyi bilinen bir nesne bulunmuyorsa, bu yöntemlerden hiçbiri uygulanamaz. Bu çalışmanın amacı, uzaklıkları bilinen pulsarlar sayesinde oluşturulan istatistiksel ilişkiler kullanılarak radyo-sessiz pulsarların uzaklık değerlerini elde etmektir.

Bu çalışmada, radyo-sessiz pulsarların uzaklıklarını elde etmek için iki farklı yöntem kullanılmıştır. İlk yöntem, gama ışını yayma verimliliğine bağlı olarak altı parametrenin doğrusal olarak ilişkilendirildiği istatistiksel bir yaklaşımı benimser. Elde edilen en uyumlu parametreler, radyo-sessiz pulsarların gama-ışını yayma verimliliğini hesaplamak için kullanılır ve bu verimlilikler daha sonra mesafe değerlerine dönüştürülür.

İkinci yöntemde ise, gama-ışını pulsarlarının çeşitli parametreleri ile parlaklıkları ara-

sında ilişki olduğunu belirten, teorik ancak gözlem ile tutarlı üç denklem kullanılmaktadır. Bu yeni denklemler, pulsarların parlaklık değerleriyle olan doğrusal bağlantısını tespit etmek üzere yeniden analiz edildi. Sonuçta ortaya çıkan uyum parametreleri, radyo-sessiz pulsarların parlaklıklarını ve mesafelerini tayin etmek için kullanıldı.

Birinci yöntemde 75 pulsarın, ikinci yöntemde ise 195 pulsarın uyum katsayılarını kullanarak 62 radyo-sessiz pulsar için uzaklık değerleri elde ettiğimiz bu çalışmada, ilk yöntemin basitliği ve istatistiksel doğası nedeniyle ilk sonuçlar zayıf performans göstermiş olsa da, ikinci yöntemle umut vadeden uzaklık değerleri elde edilmiştir.

Anahtar Kelimeler: Atarca, Gama ışınımı, Uzaklık Tahmini

Dedicated to my younger self, who aspired to be a scientist.

ACKNOWLEDGMENTS

I would like to express my deepest appreciation to my advisors, Assoc. Prof. Dr. Sinan Kaan Yerli and Assoc. Prof. Dr. Tülün Ergin Gürcan, for their invaluable guidance and support in making this thesis possible.

I am extremely grateful to Dr. Ekrem Oğuzhan Angüner for his insightful explanations and instructions throughout the analysis process of this study. I would not have been able to complete, let alone start, this thesis without his help, and I will be forever indebted to him for his contributions.

Special thanks to Assoc. Prof. Dr. Özgür Baştürk for introducing me to the scientific community with his infectious enthusiasm and for including me in his many projects over the years. His support has been instrumental in helping me become someone capable of handling a task as significant as this thesis.

I want to extend my heartfelt thanks to my friends Ege Tunç and Berfin Mina Meşe for their invaluable assistance with writing of my thesis and navigating the submission process.

TABLE OF CONTENTS

ABSTRACT v

ÖZ vii

ACKNOWLEDGMENTS x

TABLE OF CONTENTS xi

LIST OF TABLES xiii

LIST OF FIGURES xiv

LIST OF ABBREVIATIONS xvi

CHAPTERS

1 INTRODUCTION 1

1.1 Pulsars 1

1.1.1 Important Pulsar Parameters and Models 3

1.2 Observation of Pulsars 6

1.2.1 Radio Observations 6

1.2.2 Gamma-ray Observations and Fermi-LAT 7

1.3 Distance Measurements of Pulsars 9

1.4 Motivation of the Study and Definition of the Problem 12

1.4.1 Wang's Approach 13

1.4.2 Fundamental Plane Approach 14

2 METHODOLOGY 19
2.1 Linear Regression and Fit Analysis 19
2.2 Data analysis 21
2.2.1 Wang's Approach 21
2.2.2 Fundamental Plane Approach 22
3 RESULTS AND DISCUSSION FOR WANG'S APPROACH 27
4 RESULTS AND DISCUSSION FOR FUNDAMENTAL PLANE APPROACH 35
5 CONCLUSIONS 45
REFERENCES 50
APPENDIX 51
A Table of Pulsars Used in Analysis 51

LIST OF TABLES

TABLES

Table 2.1 Comparison between 4 sets of SEDs and results from Fundamental Plane Approach. 24

Table 3.1 Fit constants and adjusted R-squared values of linear fits on Wang's Approach. 28

Table 3.2 Calculated distance values (kpc) using Wang's Approach. 31

Table 4.1 Fit results for equations FP-1 (Eq. 2.3), FP-2 (Eq. 2.4) and FP-3 (Eq. 2.5). 36

Table 4.2 Calculated distance values of 62 pulsars using FP-1 and FP-2. 41

Table A.1 195 pulsars with known distance values and their relevant parameters used in this study. 52

Table A.2 62 pulsars with unknown distance values and their relevant parameters used in this study. 60

LIST OF FIGURES

FIGURES

Figure 1.1 Illustration of light cylinder and magnetic field lines. 4

Figure 1.2 Entire sky seen by Fermi-LAT. 8

Figure 1.3 SED plot of Pulsar J0007+7303. 15

Figure 1.4 Calculation of ϵ_{10} using the SED plot. The energy value corresponding to one-tenth of the peak flux is defined as ϵ_{10}. 16

Figure 2.1 A simple example of linear regression. 20

Figure 2.2 Gamma-ray emission efficiency (η) of 75 young pulsars plotted against period (P), characteristic age (τ), the magnetic field at light cylinder (B_{LC}) and generation order parameters ζ_1, ζ_2 and ζ_3 in logarithmic form. The blue dashed line represents the OLS linear regression fit. 22

Figure 3.1 Fermi 3PC distance values against the predicted distance values from the linear fit, using period (P), characteristic age (τ), magnetic field at the light cylinder (B_{LC}), and generation order parameters ζ_1, ζ_2, and ζ_3 in logarithmic form. 29

Figure 3.2 In the first two panels, we present the relative errors of the predicted distance values using the period (P), characteristic age (τ), magnetic field at the light cylinder (B_{LC}) and generation order parameters ζ_1, ζ_2, and ζ_3. 30

Figure 4.1 Distribution of variables used in FP with respect to luminosity. One can note the obvious grouping. 37

Figure 4.2 Fermi 3PC distance values versus predicted distance values using FP-1, FP-2, and FP-3 in logarithmic form. The color scheme is the same as in Fig. 3.1, and the gray dashed line represents the $x = y$ line to illustrate the distribution of the data. 38

Figure 4.3 In the top panel, we present 15-bin histograms of the relative errors of predicted distances using FP-1 and FP-2, with median values indicated in the top right corner. The bottom panel displays 30-bin histograms of the residuals of predicted distances using FP-1 and FP-2, with mean and standard deviation values shown in the top left corner. Error bars are represented by vertical red lines. 39

Figure 4.4 Histograms of the mean values of residues and median value of relative errors from 100 different "Group B" pulsar sets using FP-1 and FP-2. These histograms use 10 bins, and the mean of the data is given in the upper corners. 40

LIST OF ABBREVIATIONS

ABBREVIATIONS

FP-1	First relation from Kalapotharakos et al. (2022), in the form of Eq. 2.3
FP-2	Second relation from Kalapotharakos et al. (2022), in the form of Eq. 2.4
FP-3	Third relation from Kalapotharakos et al. (2022), in the form of Eq. 2.5
OLS	Ordinary Least Squares algorithm for statsmodels (Seabold and Perktold, 2010)
Fermi-LAT	Fermi Large Area Telescope
3PC	Third Fermi-LAT Pulsar Catalog
L_γ	Gamma Luminosity
ϵ_{cut}	Cutoff energy value
ϵ_{10}	Energy value corresponding to tenth of maximum Flux
B_*	Magnetic field at star's surface
B_{LC}	Magnetic field at light cylinder
$\dot{E}$	Spin down power
P	Period
R_{LC}	Radius of light cylinder
$\dot{P}$	Time derivative of period
τ	Characteristic age of pulsar
ζ_1	First generation order parameter proposed by Wang (2011)
ζ_2	Second generation order parameter proposed by Wang (2011)
ζ_3	Third generation order parameter proposed by Wang (2011)

SED	Spectral Energy Distribution plot
GeV	Giga electron volts
T	Tesla, the unit of magnetic flux density
ECPL	Exponential cutoff power law
4FGL	Fourth Fermi Gamma-ray LAT (Large Area Telescope) Source Catalog

CHAPTER 1

INTRODUCTION

1.1 Pulsars

Pulsars are neutron stars, dense remnants formed from the cores of massive stars that have exploded as supernovae at the end of their life cycles. These stars typically have radii of about 10 kilometers and masses around 10^{30} kilograms, resulting in an average density comparable to that of an atomic nucleus. Pulsars possess extremely strong magnetic fields, reaching up to 10^{10} T, and each rotates with a period ranging from milliseconds to about 10 seconds (Adelsberg et al., 2017). They emit beams of radio waves from their magnetic poles, which are not aligned with their rotational axis. As the pulsar spins, these beams sweep through space. If one of these beams crosses the Earth's line of sight, we observe a pulse of evenly spaced radio waves with each rotation. Consequently, we can detect roughly 20% of all pulsars, depending on their orientation relative to Earth. Pulsars were first discovered in 1967 by astronomers Antony Hewish and Jocelyn Bell (Hewish et al., 1968) at the University of Cambridge, using a radio telescope designed to record rapid radio source fluctuations. Since then, 3,724 (Australia Telescope National Facility, 2024) pulsars have been discovered, with a significant number concentrated toward the plane of the Milky Way Galaxy, our home galaxy (Adelsberg et al., 2017).

Pulsars are characterized by their highly regular rotational periods, which can range from a few milliseconds to several seconds. These periods result directly from the rotation of the neutron star itself, and each pulsar has a unique period that can be extremely stable. Millisecond pulsars, which have the shortest periods, can rotate hundreds of times per second, making them some of the fastest-spinning objects known

in the universe. The stability of pulsar periods allows them to be used as precise cosmic clocks, useful for various applications, including testing the general theory of relativity and detecting gravitational waves. Over time, pulsars tend to slow down due to the emission of electromagnetic radiation, although this spin-down rate is typically very gradual (Manchester, 2017).

Pulsars can be broadly categorized based on the primary type of electromagnetic radiation they emit: radio, X-ray, and gamma-ray pulsars. Radio pulsars are the most commonly observed type, emitting radio waves detectable with ground-based radio telescopes. They were the first type of pulsar discovered and are characterized by their regular radio pulses, which result from the rotation of the neutron star and the alignment of its magnetic and rotational axes. X-ray pulsars are typically found in binary systems, where the neutron star accretes matter from a companion star. The in-falling material heats up and emits X-rays as it approaches the neutron star's magnetic poles. These pulsars are often identified through their periodic X-ray emissions, which can be observed with space-based X-ray telescopes. Gamma-ray pulsars emit primarily in the gamma-ray part of the spectrum and are detected by space observatories like the Fermi Gamma-ray Space Telescope (Fermi) (Smith et al., 2023). These pulsars are often young and energetic, with high magnetic fields, and their gamma-ray emissions are thought to be produced by particles accelerated to high energies near the pulsar's magnetic poles (Thompson, 2001).

"Radio-quiet" or "radio-faint" pulsars, are a subclass of neutron stars that predominantly emit in the gamma-ray part of the spectrum and lack significant radio emissions. These pulsars are identified primarily through observations with space-based gamma-ray telescopes, such as Fermi. The absence of detectable radio emissions may be due to several factors, such as the orientation of the pulsar's magnetic axis relative to Earth, which could cause the radio beam to miss our line of sight. Alternatively, it may be due to intrinsic properties of the pulsar, such as weaker magnetic fields or different emission mechanisms compared to typical radio pulsars. Gamma-ray-only pulsars provide a unique opportunity to study the high-energy processes occurring in the magnetospheres of neutron stars and contribute to our understanding of particle acceleration and emission mechanisms in extreme environments (Abdo et al., 2013).

1.1.1 Important Pulsar Parameters and Models

Pulsars have many parameters that are observed or derived from other observed parameters. However, only a few of these parameters are relevant to this study, which needs further introduction.

The simplest such parameter is the period of the pulsar, usually denoted by P. It is defined as the time required for a pulsar to complete its rotation around itself, which we can measure from the time between observed pulses. As previously mentioned, this value can vary significantly depending on the pulsar but gives us two important subgroups of pulsars. Millisecond pulsars are a subclass of pulsars characterized by their exceptionally fast rotation periods, typically ranging from 1 to 10 milliseconds. They are believed to be older pulsars that have been spun up by accreting matter from a companion star in a binary system, a process known as "recycling." Non-millisecond pulsars, on the other hand, have longer rotational periods that range from about 0.1 to several seconds. These pulsars are generally younger and have not undergone the recycling process that millisecond pulsars have. For this reason, non-millisecond pulsars are also known as "young pulsars". The differences in their rotational periods reflect their different evolutionary stages and the mechanisms through which they gain or lose angular momentum (Kramer et al., 2016).

The characteristic age of a pulsar (denoted by τ) is an estimate of how long the pulsar has been emitting radiation, based on its observed spin-down rate. It provides a rough idea of the pulsar's age by assuming that the pulsar has been losing rotational energy at a constant rate due to magnetic braking. This estimate is derived from the pulsar's current rotational period (P) and its rate of slowing down ($\dot{P}$). However, the characteristic age can be imprecise because it assumes a constant braking process and does not account for variations in the pulsar's magnetic field, other energy loss mechanisms, or sudden change in the pulsar period known as 'glitch' (Taylor and Manchester, 2016).

The light cylinder (see Fig. 1.1) is an imaginary cylindrical surface centered on the pulsar's rotation axis. Within the light cylinder, magnetic field lines rotate at the same angular velocity as the pulsar itself. As you move outward from the pulsar's surface,

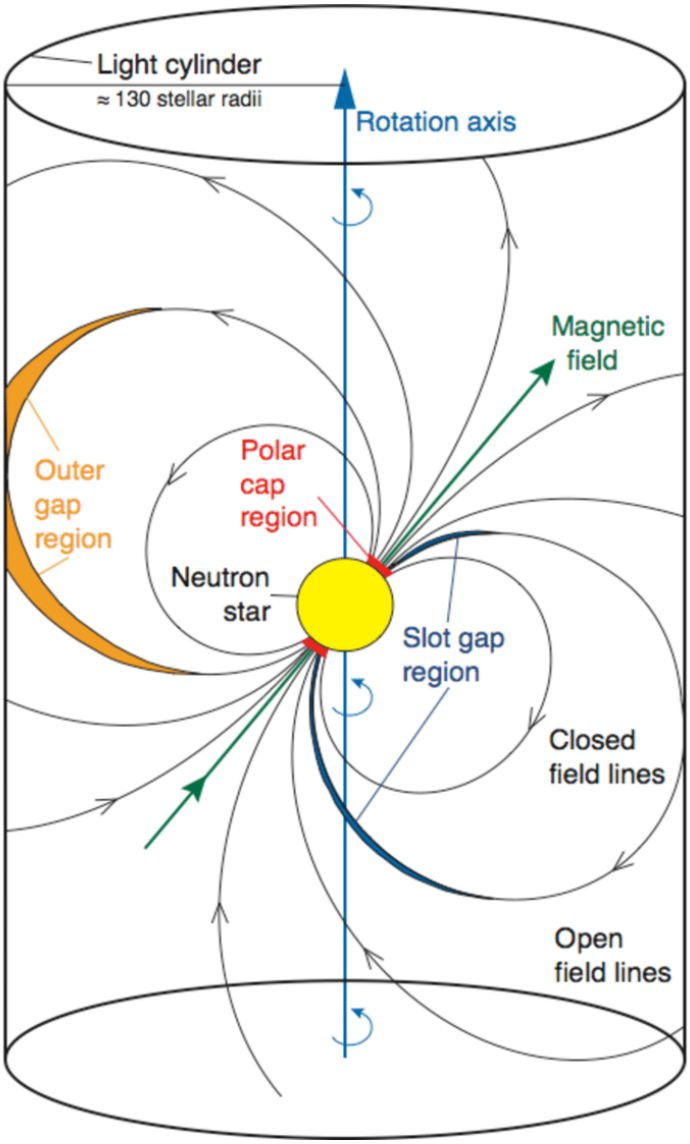


Figure 1.1: Illustration of light cylinder and magnetic field lines. Credit: Aliu et al. (2008)

the linear speed of these field lines increases until it reaches the speed of light at the light cylinder. Due to this definition its radius is determined by the distance from the pulsar at which the rotational speed of the magnetic field lines equals the speed of light. As a result, two important magnetic field values emerge, magnetic field at the light cylinder (denoted by B_{LC}) and magnetic field at star's surface (denoted by B_*). Since the magnetic field decreases with the inverse cube law, these two parameters are in direct relationship with each other (Johnston and Bailes, 2018).

As magnetic dipole radiation releases rotational energy in pulsars, it gradually lengthens the period of a pulsar which gives us two more parameters. The rate of change of period can be shown as a dimensionless number in terms of first degree time derivative of period (denoted as $\dot{P}$) and the rate of change in rotational energy over time can be shown as $\dot{E} = -I\Omega\dot{\Omega}$ where I is the moment of inertia of the pulsar (which is taken to be $10^{45} gcm^2$), Ω and $\dot{\Omega}$ are angular velocity of the pulsar and its rate of change. $\dot{E}$ is called "spin-down power" and has units of ergs per second. Even though it shares the definition and unit of luminosity, it is not measured luminosity, but rather "presumed" to be equal to luminosity of magnetic dipole radiation. For this reason, it is sometimes called "spin-down luminosity" (Johnston and Bailes, 2018).

To accurately determine the period derivative and spin-down power, Shklovskii corrections (Shklovskii, 1970) are essential. These corrections account for the impact of a pulsar's proper motion on the observed period derivative. When a pulsar has a significant transverse velocity relative to the observer, the Doppler effect can cause the observed rate of period increase to be higher than its true value. This results in an overestimation of the period derivative, which can skew the calculations of the pulsar's actual spin-down rate and intrinsic properties. Shklovskii corrections adjust for this effect by factoring in the pulsar's motion, ensuring that the period derivative more accurately reflects the pulsar's true spin-down rate. Such corrections are crucial for precise measurements of the pulsar's age, magnetic field strength, and other fundamental characteristics.

Another important topic is the two main emission models associated with pulsars, namely the polar-cap model (Sturrock, 1983) and the outer gap model (Hardcastle et al., 1995). The polar-cap and outer-gap models offer distinct explanations for pulsar emission mechanisms (see Fig. 1.1).

The polar-cap model posits that pulsar emissions originate from the magnetic poles of the neutron star, where the strong magnetic field accelerates charged particles to high energies. These particles then emit radiation as they travel along the magnetic field lines near the poles, resulting in narrow pulse profiles that are closely linked to the magnetic field geometry and the pulsar's viewing angle. This model is particularly effective in explaining pulsars with high magnetic fields and relatively simple

emission patterns. However, this model encounters limitations when it comes to explaining the existence of radio-quiet pulsars. Since the model predicts narrow pulse profiles, which would include all types of radiation the pulsar is emitting, and radio-quiet pulsars have no radio emissions, these pulsars are in direct contradiction with the model (Arons, 2019).

In contrast, the outer-gap model suggests that emission arises from regions farther from the magnetic poles, specifically in the outer gaps of the magnetosphere, which are located closer to the light cylinder. In these outer gaps, particles are accelerated by strong electric fields, and the twisted magnetic field lines contribute to the emission process. This model is better suited for explaining pulsars with broader and more complex pulse profiles, as well as those exhibiting intricate emission patterns and larger inclination angles. When it comes to radio-quiet pulsars, this model accounts for the possibility that some pulsars might be radio-quiet due to the orientation of their magnetic and rotational axes or the specific geometry of their emission regions. Thus, the outer-gap model offers a more comprehensive explanation for the wide range of pulsar behaviors, including those that do not fit well within the polar-cap model's predictions (Arons, 2019).

1.2 Observation of Pulsars

1.2.1 Radio Observations

The Australia Telescope National Facility (ATNF) is a premier radio astronomy research facility operated by CSIRO, Australia's national science agency. The ATNF provides state-of-the-art radio telescope facilities and infrastructure for both Australian and international astronomers (Australia Telescope National Facility, 2024).

The ATNF comprises several key components, each contributing uniquely to radio astronomy. The Parkes Radio Telescope (Australia Telescope National Facility, 2024), a 64-meter single-dish telescope in New South Wales, is famous for its role in the Apollo 11 moon landing and supports research on pulsars and galaxies. The Australia Telescope Compact Array (ATCA) (Australia Telescope National Facility, 2024),

near Narrabri, New South Wales, consists of six 22-meter antennas that provide high-resolution imaging of galaxies, quasars, and interstellar gas. The Mopra Telescope (Australia Telescope National Facility, 2024), a 22-meter dish near Coonabarabran, New South Wales, focuses on millimeter-wavelength observations of interstellar gas and star formation. The Australian Square Kilometre Array Pathfinder (ASKAP) (Australia Telescope National Facility, 2024), located in Western Australia's Murchison Radio-astronomy Observatory, features 36 antennas with Phased Array Feeds (PAFs) for wide-field sky surveys and supports the development of the Square Kilometre Array (SKA) project. Together, these components enable groundbreaking research and technological advancements in radio astronomy.

The ATNF Pulsar Catalog is a comprehensive database maintained by ATNF, providing detailed information on known radio pulsars. It includes data on their positions, periods, period derivatives, and other key characteristics. The catalog serves as a vital resource for astronomers studying pulsars, aiding in the analysis of their properties, distribution, and behavior. Regularly updated with new discoveries, it supports a wide range of research in astrophysics and enhances our understanding of these fascinating celestial objects (Australia Telescope National Facility, 2024).

1.2.2 Gamma-ray Observations and Fermi-LAT

Gamma-ray astronomy is the study of the non-thermal universe through the observation of gamma rays, the highest-energy form of electromagnetic radiation. Unlike visible light or radio waves, gamma rays originate from the most energetic and extreme environments in the cosmos, such as supernova explosions, neutron stars, black holes, and regions of intense stellar formation. Due to their high energy, gamma rays can penetrate thick layers of matter and are often produced in processes involving particle acceleration to relativistic speeds. Detecting gamma rays requires specialized space-based telescopes and ground-based observatories equipped with sophisticated detectors. Gamma-ray astronomy provides critical insights into the fundamental processes driving cosmic phenomena and contributes to our understanding of particle physics, cosmology, and the evolution of the universe (Longo and et al., 2011).

Fermi is a space-based observatory launched by NASA in 2008. The Large Area

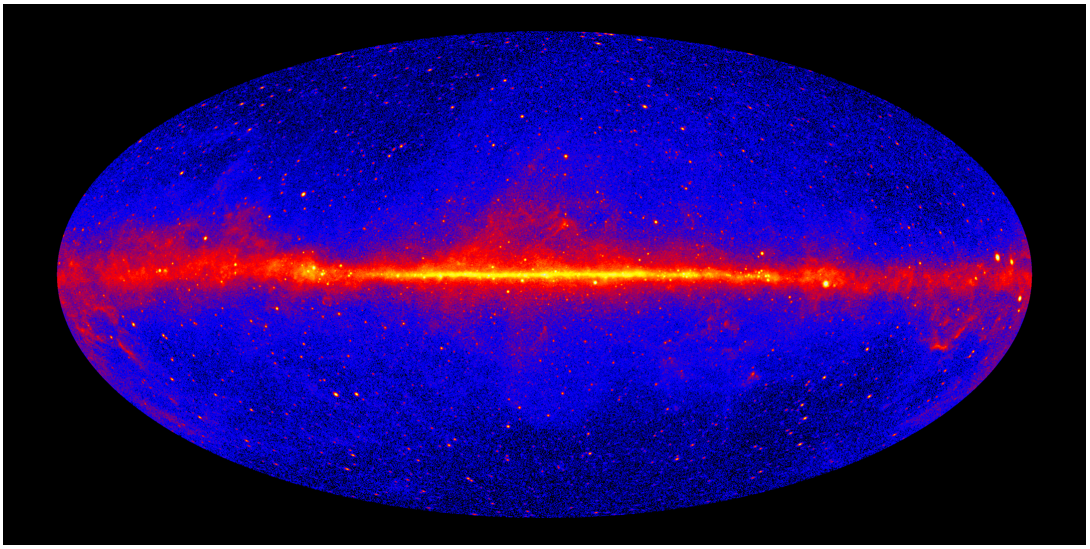


Figure 1.2: Entire sky seen by Fermi-LAT. Credit: NASA/DOE/Fermi LAT Collaboration.

Telescope (Fermi-LAT) on board Fermi operates in the energy range of about 20 MeV to 300 GeV. Fermi is designed to detect and study gamma rays from various cosmic sources, including pulsars, supernova remnants, active galactic nuclei, and gamma-ray bursts. The Fermi-LAT has significantly expanded our understanding of high-energy astrophysical phenomena by providing detailed observations of the gamma-ray sky with unprecedented sensitivity and resolution. One of its key contributions is the Fermi-LAT Pulsar Catalog, which catalogs pulsars detected by the telescope. The Fermi-LAT 3rd Pulsar Catalog (3PC) is an extensive compilation of gamma-ray pulsars, released as part of the Fermi mission, this catalog provides detailed data on 294 pulsars, significantly enhancing our understanding of these highly energetic celestial objects. The catalog also classifies pulsars based on their emission properties and includes both young, rotation-powered pulsars and older, millisecond pulsars. The Fermi-LAT 3PC serves as a critical resource for astrophysicists, enabling in-depth studies of pulsar populations, their evolution, and their role in the broader context of high-energy astrophysics. By systematically cataloging these gamma-ray sources, the 3PC has paved the way for new discoveries and a deeper understanding of the dynamic processes governing pulsars and their environments (Smith et al., 2023).

Fermi-LAT 3PC also gives us particularly important information about gamma-ray

pulsars in the form of pulsed average spectral energy distribution (SED). A pulsed average SED graph provides a comprehensive view of how a pulsar emits energy across across different gamma-ray energies. Typically plotted with energy on the horizontal axis and flux density on the vertical axis, the SED graph showcases the intensity of emission at the gamma band. Key features of SEDs include spectral peaks that indicate the frequencies where the pulsar emits the most energy, revealing insights into its emission mechanisms and the structure of its magnetic field. SEDs often exhibit exponential cutoff power-law behavior, showing how the flux density changes with energy and highlighting different emission processes such as synchrotron radiation or curvature radiation. Breaks or turnovers in the SEDs can signify transitions between emission mechanisms, providing clues about the physical conditions within the pulsar's magnetosphere. By studying the SED, astronomers can discern the nature of the pulsar's emission, its particle acceleration mechanisms, and its role in the broader context of high-energy astrophysics (Smith et al., 2023).

1.3 Distance Measurements of Pulsars

To talk about distance measurement of any kind in astronomy, we first need to introduce the cosmic distance ladder. The cosmic distance ladder is a hierarchical concept used by astronomers to scale distances to celestial objects across the universe, ranging from nearby planets and stars to distant galaxies and the cosmic microwave background. It consists of various techniques and observations, each building upon the next to extend our measurement capabilities. At its foundation are direct measurements within our solar system, such as radar ranging to planets and spacecraft observations. Moving outward, parallax measurements rely on observing how nearby stars appear to shift against more distant background stars as Earth orbits the Sun. Beyond the range of parallax, astronomers use standard candles like Cepheid variables and Type Ia supernovae, whose intrinsic brightness can be inferred from their periodicity or light curves. These measurements calibrate distance indicators used for galaxies and clusters, employing techniques such as red-shift measurements from spectroscopy to gauge cosmic expansion. Ultimately, the cosmic distance ladder serves as a critical tool in mapping the universe's vast distances and understanding

its structure and evolution (Weinberg, 2008).

Measuring the distances to pulsars, which are compact and often located far from Earth, requires sophisticated astronomical techniques. Several methods are employed in combination to achieve accurate distance determinations:

Similar to measuring parallax for nearby stars, pulsar parallax relies on observing the apparent shift in the position of a pulsar against the background of distant stars as Earth orbits the Sun. This shift, known as annual parallax, results in a slight apparent change in the pulsar's position due to Earth's changing vantage point. By measuring this angular shift and knowing the Earth's orbital parameters, astronomers can calculate the pulsar's distance. Although pulsar parallax measurements typically provide distances to pulsars within a few thousand light-years, they are still crucial for calibrating other distance measurement techniques (Kramer and Wex, 2020).

The dispersion measure (DM) of a pulsar, which quantifies how much the pulsar's radio waves are dispersed as they travel through the interstellar medium, is directly proportional to the distance squared. By measuring the DM and using models of the distribution of electrons in the Milky Way, astronomers can estimate the distance to the pulsar. This method is particularly effective for pulsars with known distances or for statistical studies across large populations of pulsars (Kramer and Wex, 2020). For this method, astronomers usually make use of NE2001 (Cordes and Lazio, 2002) and YML16 (Yao et al., 2016) electron density models.

The NE2001 electron density model is developed by Cordes and Lazio (2002), and it is a widely used electron density model for the Galactic interstellar medium. It incorporates observations from pulsar dispersion measures and other data to provide a comprehensive description of the electron density distribution in the Milky Way. The model divides the Galaxy into different components, including a disk and halo, and uses parameterized functions to describe the electron density in these regions. The NE2001 model has been particularly influential in pulsar research and in studies of the interstellar medium due to its detailed and structured approach.

The YML16 electron density model, on the other hand, is introduced by Yao et al. (2016), and uses a three-dimensional model of the Galactic electron density that im-

proves upon previous models by incorporating new data from pulsar dispersion measures and other sources. It provides a more detailed and accurate representation of the distribution of free electrons in the interstellar medium, particularly in the Galactic plane and towards the Galactic center. The model uses a combination of parametric forms and observational data to account for variations in electron density across different regions of the Galaxy, making it a valuable tool for studying pulsars, interstellar medium properties, and the structure of the Milky Way.

Pulsar timing is another powerful technique where precise measurements of the arrival times of pulsar pulses over long periods reveal deviations caused by the pulsar's motion in its orbit, often around a companion star. By analyzing these timing variations, astronomers can derive the pulsar's orbital parameters, including its distance, with high precision. This method is especially useful for pulsars in binary systems, where the companion star's properties can further constrain the distance determination (Kramer and Wex, 2020).

Some pulsars are associated with supernova remnants or globular clusters, whose distances can be independently measured through other methods, such as observations of their stars or variable stars. By establishing these associations and determining the distances to the parent objects, astronomers can infer the distances to the pulsars themselves (Kramer and Wex, 2020).

Pulsars, particularly those moving through the Galaxy at high velocities, can be used as tracers of the galactic structure. By modeling their motions and velocities, combined with knowledge of the Milky Way's rotation curve, astronomers can estimate their distances. This approach, known as the kinematic distance method, provides insights into the pulsar's origin and the dynamics of the Milky Way (Kramer and Wex, 2020).

The measurement of pulsar distances holds significant importance in several key areas of astrophysics. First, pulsars are essential tools for testing fundamental physics, including the properties of dense matter and the behavior of gravitational waves. Accurate distances help refine these tests, providing insights into neutron star interiors and gravitational wave propagation. Second, pulsars are vital for studying the interstellar medium; their emission properties vary with distance, allowing astronomers to

probe the distribution of ionized gas and magnetic fields. Third, pulsars are crucial for understanding the structure and evolution of the Galaxy and beyond. By mapping their positions accurately, astronomers can trace the Galactic spiral arms, explore star formation history, and even identify the presence of unseen dark matter. Therefore, precise measurements of pulsar distances not only deepen our understanding of neutron stars and their environments but also contribute to broader advancements in astrophysics and cosmology (Kramer and Wex, 2020).

1.4 Motivation of the Study and Definition of the Problem

Measuring the distances of radio-quiet pulsars, such as X-ray or gamma-ray pulsars, presents significant challenges due to their unique observational characteristics and the limitations of current detection methods. Unlike radio pulsars, which emit detectable radio waves used for precise timing and parallax measurements, radio-quiet pulsars lack such emissions, rendering traditional pulsar timing techniques ineffective. This absence complicates the direct measurement of distances through methods commonly employed for radio pulsars. Identifying and localizing radio-quiet pulsars within the sky also proves challenging, as they typically require space-based telescopes with limited spatial resolution compared to radio telescopes. Thus, accurately pinpointing their positions and subsequently determining distances becomes more difficult. Distance indicators must rely on alternative methods, such as associations with supernova remnants or globular clusters, but these associations can be ambiguous and subject to uncertainties in distance estimates for associated objects. Moreover, the complex modeling of X-ray and gamma-ray emissions from pulsars, coupled with interstellar absorption and scattering effects, introduces additional uncertainties into distance calculations. The aim of this study is to overcome these difficulties of pulsar distance measurements by utilizing two main methods, namely "Wang's Approach" by Wang (2011) and "Fundamental Plane Approach" by Kalapotharakos et al. (2022) to predict approximate distance values of radio-quiet pulsars.

1.4.1 Wang's Approach

To overcome these challenges in distance measurements of radio-quiet pulsars, Wang (2011) proposed a statistical approach. In his study, he provides a background on the relationship between X-ray luminosity and a pulsar's spin-down power which varies depending on the energy band. In soft X-ray bands (0.1 – 2.4 keV), the luminosity L_x is proportional to the spin-down power $\dot{E}$ (Becker and Truemper, 1997). In harder X-ray bands (> 2 keV), however, studies by Saito (1998) and Cheng et al. (2004) suggest that L_x scales with $\dot{E}^{3/2}$. Later on, Thompson et al. (1999) observed a potential correlation between gamma-ray luminosity $L_\gamma \propto \dot{E}^{1/2}$. Abdo et al. (2010) extended this analysis to a larger sample of gamma-ray pulsars, finding that while young pulsars generally follow this relation with considerable scatter, millisecond pulsars exhibit a different pattern.

Wang (2011) pointed out how the efficiency of gamma-ray emission ($\eta = L_\gamma/\dot{E}$) is a crucial parameter for understanding gamma-ray pulsars, as it varies across different pulsar populations. His study focused on examining how gamma-ray emission efficiency relates to various pulsar parameters: spin period (P), characteristic age (τ), magnetic field at the light cylinder (B_{LC}), and three generation order parameters ($\zeta_1, \zeta_2, \zeta_3$). These generation order parameters are functions of period and its derivative and they are associated with various emission mechanics that we observe from the pulsar, which are derived assuming the gamma-ray emission is compatible with polar cap model. By plotting these six parameters against gamma-ray emission efficiency, he searched for a linear relation between them. If these plots revealed a linear relationship, he used the fitted linear function to calculate the gamma-ray emission efficiency of gamma-ray pulsars that had no distance values. Since gamma-ray emission efficiency depends only on luminosity and spin-down power ($\eta = L_\gamma/\dot{E}$), by using the spin-down power from the pulsar catalog, he calculated the luminosity values and converted them to distance values using the formula:

$$L_\gamma = 4\pi d^2 f_\Omega F_\gamma \tag{1.1}$$

Here L_γ is gamma-ray luminosity, d is distance, F_γ is gamma-ray flux above 100 MeV

detected by Fermi-LAT and f_Ω is the radiation open angle factor (Wang, 2011). f_Ω is a model dependent variable and can vary based on magnetic inclination and observer angles. Watters et al. (2009) found $f_\Omega \sim 1$ for 8 gamma-ray pulsars and Abdo et al. (2010) assumed $f_\Omega = 1$ for its calculations. For this reason, cite2011RAA....11..824W also assumes $f_\Omega = 1$ in this study.

His study finds two promising linear relations, one between gamma-ray emission efficiency and magnetic field at light cylinder, and the other between gamma-ray emission efficiency and third generation order parameter, which he notes as showing stronger correlation. He concludes that these new relations can be used as a new possible method to predict the distance values of radio-quiet pulsars.

1.4.2 Fundamental Plane Approach

However, two papers by Kalapotharakos et al. (2019) and Kalapotharakos et al. (2022) introduce a new theoretical relation between gamma-ray observables.

$$L_\gamma \propto \epsilon_{cut}^{4/3} B_*^{1/6} \dot{E}^{5/12}. \tag{1.2}$$

Here L_γ is the gamma-ray luminosity, $\dot{E}$ is spin-down power, B_* is the magnetic field at star's surface and ϵ_{cut} is the cutoff energy value, which is defined to be the energy value in SED plots, where the curve starts to decrease exponentially. They derived this relationship under the assumption that the pulsar's gamma-ray emission results from curvature radiation produced by particles accelerated at the equatorial current sheet just beyond the light cylinder. Although this new relation has familiar variables, the process of obtaining energy cutoff value requires preliminary fitting of SED to the exponential cutoff power law (ECPL) model given in the following formula:

$$\epsilon^2 \frac{dN}{d\epsilon} = A\epsilon^{2-\Gamma} exp[-(\frac{\epsilon}{\epsilon_{cut}})^b] \tag{1.3}$$

Here, ϵ is the photon energy $dN/d\epsilon$ is the number of photons in an energy bin, Γ is the photon index, b describes the strength of decay of the emitted power at high energies and A is flux normalization. For some pulsars, these b values are given in the Fermi pulsar catalog and for those pulsars that do not have this value, b is

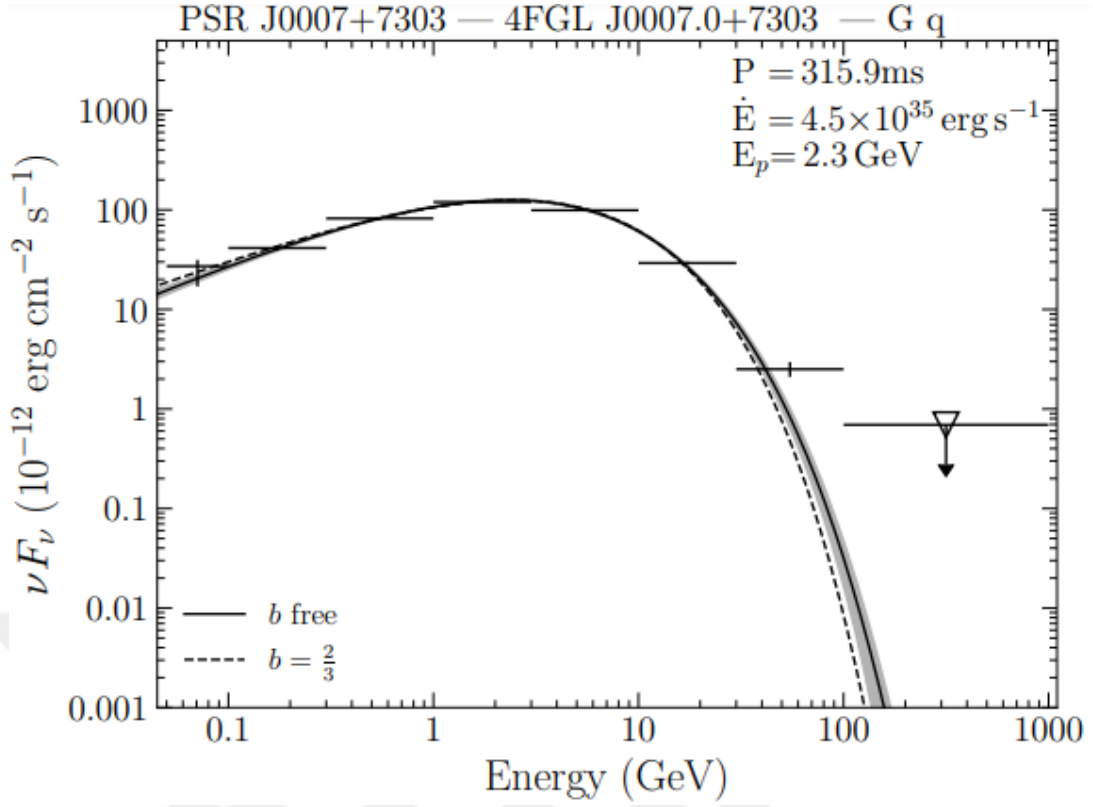


Figure 1.3: SED plot of Pulsar J0007+7303. The SED flux data are given with 1 sigma errors from the Fermi catalog. Solid and dashed lines are models assuming $b = 2/3$ and $b = 1$ respectively, while gray shaded region is 1 sigma error interval of $b = 1$ model. Due to high error margins in the observation, last observed data point with the downright arrow indicates an upper limit.

taken to be 2/3. Kalapotharakos et al. (2022) used model parameters provided in the Fermi 4FGL catalog to generate synthetic SED points, and derived the cutoff energy ϵ_{cut} by fitting the ECPL model given in Eq. 1.3 to the synthetic data. During these calculations, since a SED plot covers a wide range of energies and does not give relevant information after the energy cutoff point, Kalapotharakos et al. (2022) limited the energy range of the SED plot to [0.1, 15] GeV.

On top of their initial relation, Kalapotharakos et al. (2022) noted another, albeit similar candidate: ϵ_{10}. This variable is defined as the value of energy corresponding to 1/10 of the maximum flux, and behaves similarly to ϵ_{cut}. For its similar behaviour, it can replace ϵ_{cut} it in the original formula. The new relation becomes:

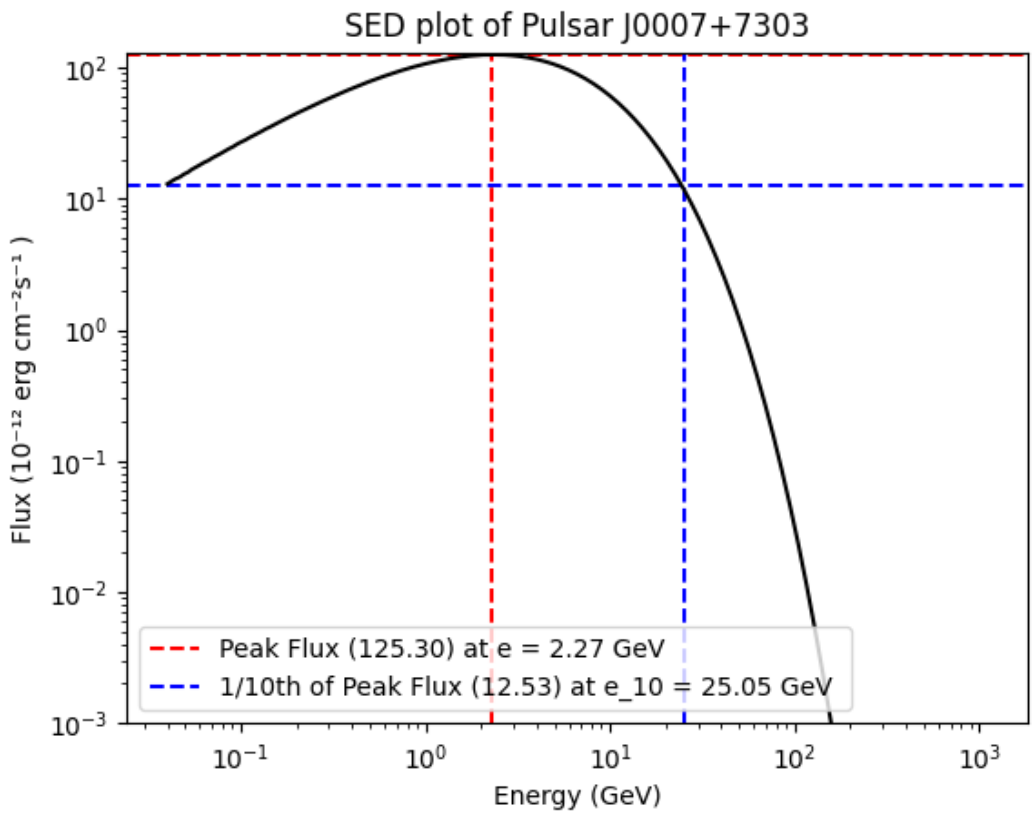


Figure 1.4: Calculation of ϵ_{10} using the SED plot. The energy value corresponding to one-tenth of the peak flux is defined as ϵ_{10}.

$$L_\gamma \propto \epsilon_{10}^{4/3} B_*^{1/6} \dot{E}^{5/12}. \tag{1.4}$$

Continuing their analysis, they also noted that B_* depends on B_{LC} with the formula

$$B_L C \propto B_* R_{LC}^{-3} \propto B_* P^{-3} \tag{1.5}$$

where R_{LC} is the radius of light cylinder. Since both B_{LC} and $\dot{E}$ depend on period P and its derivative $\dot{P}$ with the formulas:

$$\dot{E} = 4\pi^2 I \dot{P} P^{-3} \tag{1.6}$$

$$B_{LC} = 2.94x10^8 (\dot{P} P^{-5})^{1/2} \tag{1.7}$$

They ended up with the third luminosity relation:

$$L_\gamma \propto \epsilon_{cut}^{4/3} P^{-7/6} \dot{P}^{1/2}. \tag{1.8}$$

They supported these claim by fitting the data of 88 pulsars from second Fermi Pulsar Catalog (Kalapotharakos et al., 2019), and noted the remarkable accuracy of this new relation. Following their initial paper, they published another in 2022 (Kalapotharakos et al., 2022), where they reaffirmed their relation by fitting 190 pulsars from the third Fermi Pulsar Catalog. The results from the latter article for Eqs. 1.1 and 1.3 are as follows:

$$L_\gamma = 10^{14.3\pm1.3} \epsilon_{cut}^{1.39\pm0.17} B_*^{0.12\pm0.03} \dot{E}^{0.39\pm0.05}$$

$$L_\gamma = 10^{10.2\pm1.35} \epsilon_{10}^{1.22\pm0.17} B_*^{0.11\pm0.03} \dot{E}^{0.51\pm0.05}$$

This research group discovered a significant potential new relation of gamma-ray observables; however, they did not pursue this relationship further to obtain distance values for gamma-ray pulsars.

CHAPTER 2

METHODOLOGY

2.1 Linear Regression and Fit Analysis

Before we start our analysis, it is important to introduce our fit algorithm and the various parameters we use throughout this paper to measure its accuracy.

Ordinary Least Squares (OLS) is a statistical method used in linear regression to find the best-fitting line through a set of data points. The main goal of OLS is to minimize the differences (called residuals) between the observed values (actual data points) and the values predicted by the linear model. In simpler terms, OLS tries to make the predicted line as close as possible to all the actual data points by minimizing the overall error. This results in the best estimates for the model's parameters, allowing for the best prediction of the dependent variable based on the independent variables (Wooldridge, 2016).

For all the linear regression fits in this paper, we utilized Ordinary Least Squares (OLS) of `statsmodels` library by Seabold and Perktold (2010) in a Python environment.

Furthermore, R-squared (R^2) is a performance metric that indicates how well the independent variables in a regression model explain the variability of the dependent variable. It represents the proportion of the total variance in the dependent variable that is accounted for by the independent variables. R-squared values range from 0 to 1, where 0 means the model explains none of the variance and 1 means it explains all the variance. While a higher R-squared suggests a better fit, it can be misleading, especially when comparing models with different numbers of predictors. This is

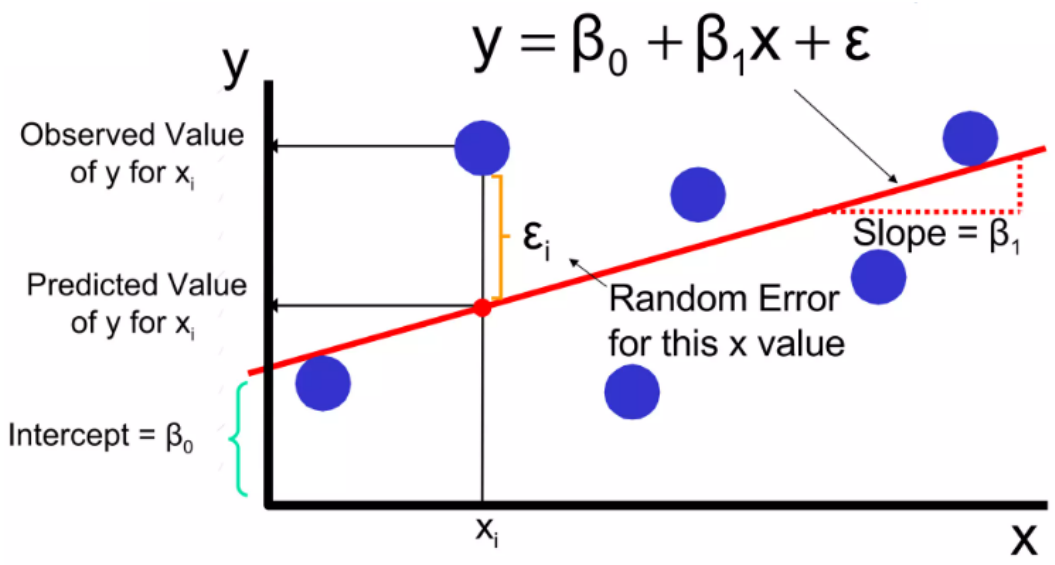


Figure 2.1: A simple example of linear regression. Adapted from the Statistical Inferences tutorial by Prof. Haris Aslam, University of Management and Technology, Lahore, Pakistan. Retrieved from [https://www.slideshare.net/CallplanetsDeveloper/class-10-linear-regressionpptx]

because R-squared always increases when more predictors are added to the model, regardless of their relevance. To address this, Adjusted R-square adjusts the R-squared value based on the number of predictors and the sample size. It accounts for the potential over-fitting by penalizing the inclusion of unnecessary predictors, providing a more accurate measure of model performance when comparing models with different numbers of predictors (Montgomery et al., 2012).

The formula of R^2 is as follows:

$$R^2 = 1 - \frac{SS_{res}}{SS_{tot}} \tag{2.1}$$

where SS_{res} is the residual sum of squares with the formula $\sum_{i=1}^{n}(y_i - \hat{y}_i)^2$ and SS_{tot} is the total sum of squares with the formula $\sum_{i=1}^{n}(y_i - \bar{y}_i)^2$. Here y_i is the observed value, $\hat{y}_i$ is the predicted value and $\bar{y}_i$ is the mean of the observed values. After calculating R^2, we can obtain R^2_{adj} with the formula:

$$R^2_{adj} = 1 - (\frac{1 - R^2}{n - p - 1})(n - 1) \tag{2.2}$$

Here, n is the number of observations (sample size) and p is the number of predictors (independent variables) in the model. Our overall aim is to calculate these R^2_{adj} values for each fit alongside the standard deviation to estimate its success.

2.2 Data analysis

In order to start our analysis, we gathered the data of 294 pulsar from the Fermi-LAT 3PC catalog (Smith et al., 2023). After careful consideration, we decided not to include 7 pulsars that lack $\dot{P}$ data due to its importance in our analysis, 20 pulsars that lack detection from Fermi-LAT analysis (no luminosity or flux data), and 8 pulsars due to the lack of significant cutoff behaviour on their SED plots (these plots were more compatible with power law). This leaves us with 120 millisecond and 75 young pulsars with known distance and 57 young and 5 millisecond pulsars with unknown distance values. All of the pulsars and their relevant parameters that are used in this study are given in the Appendix as Tables A.1 and A.2.[1]

2.2.1 Wang's Approach

Following Wang (2011) methodology, we calculated gamma-ray emission efficiency η with the formula $\eta = L_\gamma/\dot{E}$ and used OLS linear regression on 75 young pulsars using the aforementioned variables P, τ, B_{LC}, ζ_1, ζ_2, ζ_3.

To test the success of these linear fits, we calculated their adjusted R-squared values. Furthermore, we tested our linear fit on the 75 young pulsars (same pulsars we obtained the fit from) by plotting predicted distances (using Eq. 1.1) against their catalog distances around $x = y$ line. Additionally, we created two histograms to show the relative error ($|(dist_{pred} - dist_{true})|/dist_{true}$) of their predicted distances, along with their residuals ($(dist_{pred} - dist_{true})$).

[1] For $\dot{P}$ and $\dot{E}$ values, if available, Shklovskii corrected (Shklovskii, 1970) values are used. These are given in Fermi-LAT 3PC catalog (Smith et al., 2023) as "P1corr" and "EDOTcorr".

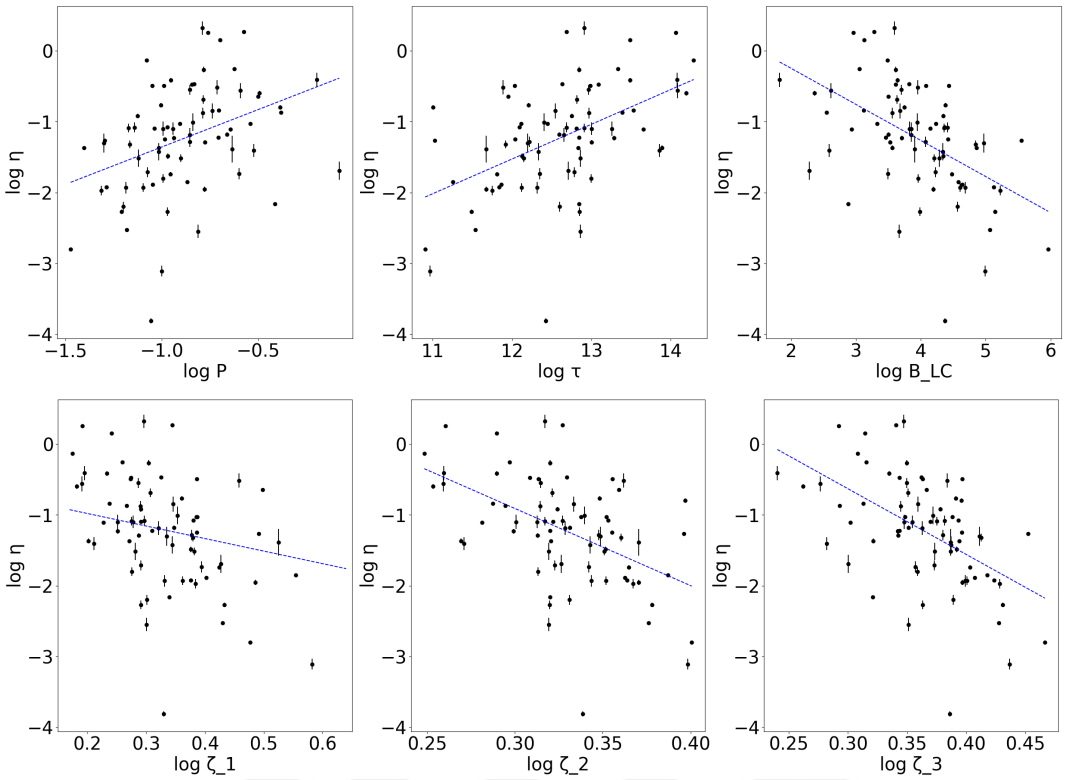


Figure 2.2: Gamma-ray emission efficiency (η) of 75 young pulsars plotted against period (P), characteristic age (τ), the magnetic field at light cylinder (B_{LC}) and generation order parameters ζ_1, ζ_2 and ζ_3 in logarithmic form. The blue dashed line represents the OLS linear regression fit.

Then we used the same linear fit coefficients to predict the gamma-ray emission efficiency of radio-quiet pulsars with unknown distance values. After calculating L_γ by using $\eta = L_\gamma/\dot{E}$ and obtaining flux values (F_γ) from the Fermi-LAT 3PC catalog, we used Eq. 1.1 to achieve our initial goal, the predicted distance values of radio-quiet pulsars.

2.2.2 Fundamental Plane Approach

Following the methodology from Kalapotharakos et al. (2022), we first needed to calculate the energy cutoff value ϵ_{cut} and ϵ_{10} from Eq. 1.3. To achieve this, we began modelling SEDs using Fermi-LAT 3PC (Smith et al., 2023) and created synthetic data

points along the observed points using the SEDPlotter provided by[2] Fermi-LAT 3PC catalog (see Fig. 1.3).

In the Fermi-LAT 3PC catalog (Smith et al., 2023), faint pulsars have fixed b values at $b = 2/3$ and brights pulsars have free b values (denoted as "bfr"). To test the effects of parameter b from Eq. 1.3 in our analysis, we generated two different sets of SED plots, namely "b23" and "hybrid". In the "b23" set, we assumed $b = 2/3$ for every pulsar, whereas in the "hybrid" set, we accepted the "bfr" parameter from the Fermi-LAT 3PC catalog as b and only assumed $b = 2/3$ for pulsars that did not have the "bfr" parameter. Then we proceeded to create two more sub sets of SED plots: one with limits of 0.04-1100 GeV, the default range in SED plotter provided by the Fermi-LAT 3PC catalog, which we called "wide", and one with limits of 0.1-15 GeV, the range used by Kalapotharakos et al. (2022), which we called "narrow". In total we ended up with four sets of SED plots: "b23 wide", "b23 narrow", "hybrid wide" and "hybrid narrow".

Using these SED plots, we proceeded to calculate ϵ_{cut} by fitting Eq. 1.3 and ϵ_{10} from the peak flux.

After obtaining all the necessary parameters, we used the log-linear form of Eq. 1.3 given as:

$$log_{10}L_\gamma = a + b\log_{10}\epsilon_{cut} + c\log_{10}B_* + d\log_{10}\dot{E}. \tag{2.3}$$

to obtain the Fundamental Plane constants a, b, c, d. [3] After analysing the results in Table 2.1 we decided to continue with the "hybrid narrow" approach, as it yielded the most promising results, and is the original approach by Kalapotharakos et al. (2022).

During this initial analysis of SED plot sets, seven pulsars were omitted due to their lack of SED plots. These seven pulsars, namely J1023+0038, J1402+1306, J1526-2744, J1627+3219, J1803-6707, J1824-0621, J2116+1345 had very few detected observational points and required manual analysis outside of SED plotter provided by the Fermi-LAT 3PC catalog. After deciding to continue with "hybrid narrow" ap-

[2] https://fermi.gsfc.nasa.gov/ssc/data/access/lat/3rd_PSR_catalog/3PC_SEDPlotter.py
[3] This Eq. will be referred as "FP-1" from now on for convenience.

Table 2.1: Comparison between 4 sets of SEDs and results from Fundamental Plane Approach. The numbers in parenthesis are their relative error given in units of standard deviation (sigma) compared to theoretical exponential constants in Eq. 1.2.

Analysis Approach	Pulsar Count	ϵ_{cut} constant b	B_* constant c	$\dot{E}$ constant d
b23 Wide	188	1.08 +/- 0.12 (2.09)	0.12 +/- 0.03 (1.77)	0.41 +/- 0.05 (0.09)
Hybrid Wide	188	0.94 +/- 0.12 (3.27)	0.11 +/- 0.03 (2.04)	0.42 +/- 0.05 (0.12)
b23 Narrow	188	1.31 +/- 0.15 (0.15)	0.13 +/- 0.03 (1.52)	0.41 +/- 0.05 (0.16)
Hybrid Narrow	188	1.27 +/- 0.16 (0.42)	0.12 +/- 0.03 (1.65)	0.42 +/- 0.05 (0.03)
FP article e_c1 results	190	1.39 +/- 0.17 (0.35)	0.12+/-0.03 (1.56)	0.35+/-0.05 (1.33)

proach, we manually analyzed and fitted these pulsars to obtain their ϵ_{cut} and e_{10} values to complete the set of values for all 195 pulsars.

Similar to what we did in Eq. 2.3, to obtain the exponential constants of Eqs. 1.4 and 1.8, we transformed the forms of these equations into:

$$log_{10}L_\gamma = a + b\log_{10}\epsilon_{cut} + clog_{10}B_* + dlog_{10}\dot{E} \tag{2.4}$$

and

$$log_{10}L_\gamma = a + b\log_{10}\epsilon_{10} + clog_{10}P + dlog_{10}\dot{P}. \tag{2.5}$$

These equations are then linearly fitted to obtain the corresponding constants. [4]

Additionally, we have decided to examine the differences between millisecond and young pulsars in our analytical approach. To achieve this, we separated the 195 pulsars into two groups and repeated the previous fits for equations FP-1, FP-2 and FP-3.

One thing to note is that, up until this point, the Fundamental Plane Approach we used was solely focused on pulsars with known luminosity and distance values. This is because we aim to quantify the accuracy of our approach before applying it to radio-quiet pulsars with unknown distance values. To achieve this, we first repeated

[4] These equations will be referred to as "FP-2" and "FP-3" respectively from now on for convenience.

the procedure from Wang's Approach, where we tested our linear fit constants on 195 pulsars with known distance values. We plotted predicted distances against their catalog distances around the $x = y$ line and created two histograms to show the distribution of relative errors and residuals of predicted distances. The median of relative errors, mean and standard deviation of residuals were calculated accordingly.

However, we know that due to the dependence of data, testing the fit against the data used to obtain the fit will result in biases. To overcome this bias, we also separated the 195 pulsars into two independent groups, called "Group A" and "Group B," with 136 (70%) and 59 (30%) pulsars, respectively. Group A was used to obtain new constants a, b, c, and d from equations FP-1, FP-2, and FP-3. With these constants, we predicted distance values for Group B and compared them to their catalog distance values. However, arbitrarily dividing the data into 70% and 30% groups might still introduce bias, depending on the pulsars in each group. Therefore, to eliminate this bias, we repeated this procedure 100 times with different randomly selected Group A and Group B. For each random selection, we calculated the median of the relative error as well as the mean of the residuals and presented their distributions in histograms.

Finally, using the constants from equations FP-1, FP-2, and FP-3 derived from 195 pulsars with known luminosity values, we estimated the luminosity values of 62 radio-quiet pulsars. Furthermore, using these luminosity values and equation 1.1, we estimated the distance values of these radio-quiet pulsars.

CHAPTER 3

RESULTS AND DISCUSSION FOR WANG'S APPROACH

Calculated R^2_{adj} values of linear fits from Wang's approach are listed in Table 3.1. Analyzing the results, we can concluded that low R^2_{adj} values indicate inadequate linear fits, which can be visually confirmed from Fig. 2.2.

When we look at the predicted distance comparisons in Fig. 3.1, we can immediately see a few outlier predictions. These outliers can be observed in Fig. 2.2 on the edges of the plot, as points that are furthest away from our linear fit. It should be no surprise that when we include these points in the fit, it results in inaccurate predictions. Additionally, we can see that our predictions do not align exactly with any particular distance measurement method, and the error bars of our predictions generally appear to be larger than their catalog counterparts.

Seeing the relative error calculations from Fig. 3.2, it becomes clear that outlier data points can cause huge deviations from the catalog distance, to the point where the predicted distance is 15 times the catalog distance. However, we can still see that most of our predictions are within a reasonable range, with median values around 0.45, which implies that 50% of our predictions have a relative error of less than 0.45. When it comes to residuals, we can see that for the period and first-order generation parameter, there is a slight overestimation of distance, whereas for the remaining parameters, we observe a slight underestimation. However, since we found lower R^2_{adj} values for these two parameters in particular, it seems they are worse candidates for predicting distance with this method. Although Wang (2011) found B_{LC} and ζ_3 parameters to give the best results, our analysis of R^2_{adj} values, relative errors, and residuals does not suggest particularly better results for these two parameters.

Table 3.1: Fit constants and adjusted R-squared values of linear fits on Wang's Approach.

Variable Used in Fit	Slope	Y-Intercept	Adjusted R-Square Value
Period (P)	1.06	-0.298	0.128
Characteristic Age (τ)	0.49	-7.41	0.237
Magnetic Field at Light Cylinder (B_LC)	-0.509	0.772	0.253
First Generation Order Parameter (ζ_1)	-1.77	-0.624	0.0664
Second Generation Order Parameter (ζ_2) (P)	-10.9	2.36	0.236
Third Generation Order Parameter (ζ_3) (P)	-9.28	2.16	0.269

Finally, we can see the distance predictions for 57 millisecond radio-quiet pulsars using Wang's Approach in Table 3. Some of these results have large error bars, which can be attributed to the weakness of single-variable linear fits and outlier data points.

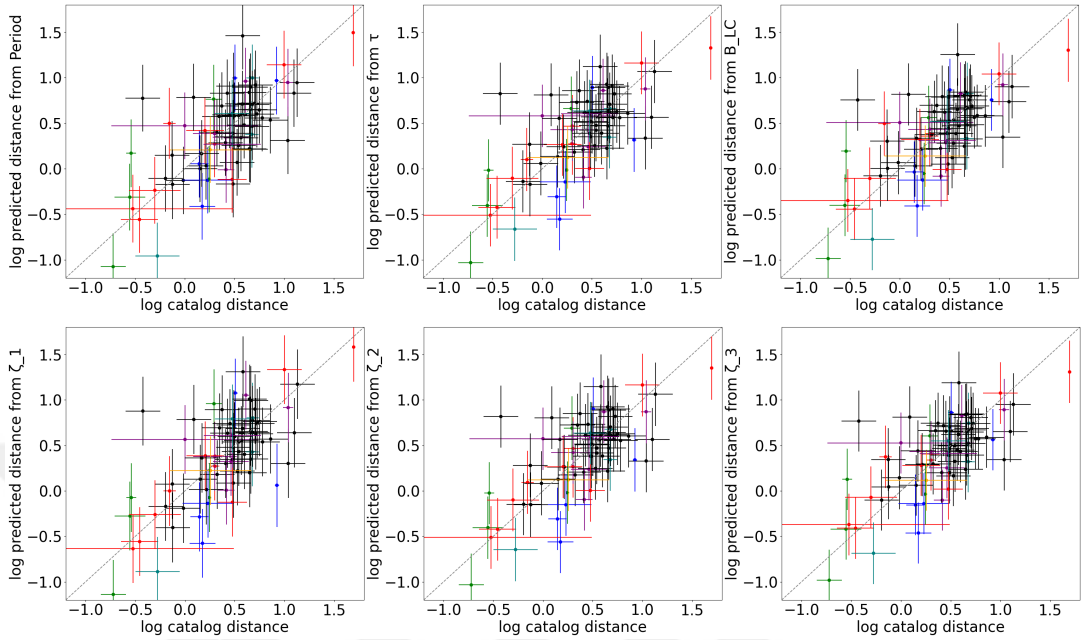


Figure 3.1: Fermi 3PC distance values against the predicted distance values from the linear fit, using period (P), characteristic age (τ), magnetic field at the light cylinder (B_{LC}), and generation order parameters ζ_1, ζ_2, and ζ_3 in logarithmic form. We used seven different colors to represent each method employed for obtaining catalog distances, enabling comparison across various distance measurement methodologies. Blue points correspond to the kinetic HI absorption method, green points to the parallax method, and black points represent the dispersion measure method using the YMW16 electron density model (Yao et al., 2016). Orange points are derived from the ATNF Pulsar Catalog (Australia Telescope National Facility, 2024), while purple points represent a combination of dispersion measure and kinetic approaches that account for the Lutz-Kelker bias (Verbiest et al., 2012). Teal points indicate X-ray hydrogen column density measurements, and red points denote optical and other methods. The gray dashed line represents the $x = y$ line to help illustrate the distribution of the data.

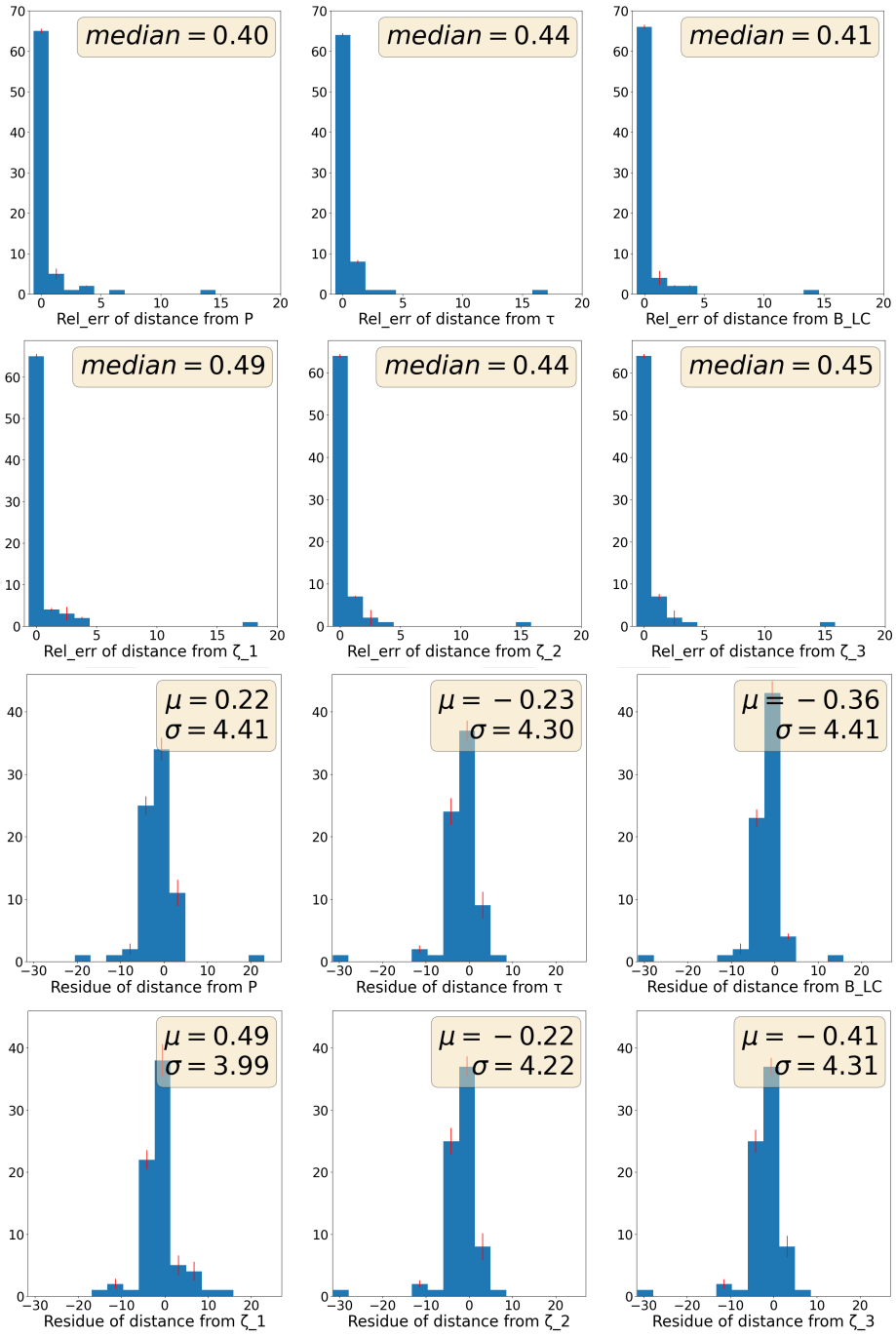


Figure 3.2: In the first two panels, we present the relative errors of the predicted distance values using the period (P), characteristic age (τ), magnetic field at the light cylinder (B_{LC}) and generation order parameters ζ_1, ζ_2, and ζ_3. The third and fourth panels contains the residuals of the predicted distance values based on same six parameters. Each histogram uses 15 bins, with error bars shown as red lines. The median value of the data is provided in the top right corner of each panel.

Table 3.2: Calculated distance values (kpc) using Wang's Approach.

Name	$Dist_P$	$Dist_\tau$	$Dist_{B_{LC}}$	$Dist_{\zeta_1}$	$Dist_{\zeta_2}$	$Dist_{\zeta_3}$
J0357+3205	0.42 ± 0.15	0.37 ± 0.79	0.54 ± 0.29	0.26 ± 0.10	0.37 ± 0.42	0.52 ± 0.49
J0359+5414	4.38 ± 2.23	5.96 ± 12.29	4.52 ± 3.07	6.22 ± 2.40	5.85 ± 7.01	4.89 ± 5.20
J0554+3107	2.37 ± 0.82	1.15 ± 2.36	2.25 ± 1.28	1.05 ± 0.47	1.13 ± 1.37	1.77 ± 1.76
J0622+3749	1.42 ± 0.52	1.16 ± 2.43	1.62 ± 0.92	0.96 ± 0.37	1.15 ± 1.33	1.50 ± 1.46
J0633+0632	1.21 ± 0.45	0.77 ± 1.58	1.18 ± 0.70	0.74 ± 0.31	0.76 ± 0.91	1.00 ± 1.01
J0734-1559	1.30 ± 0.57	1.57 ± 3.30	1.50 ± 0.92	1.36 ± 0.51	1.55 ± 1.81	1.54 ± 1.55
J0744-2525	0.96 ± 0.47	2.54 ± 5.52	1.45 ± 0.90	1.56 ± 0.53	2.64 ± 2.87	1.90 ± 1.86
J0802-5613	0.93 ± 0.36	1.38 ± 3.01	1.38 ± 0.76	0.84 ± 0.29	1.44 ± 1.56	1.59 ± 1.47
J1023-5746	5.53 ± 2.61	3.18 ± 6.25	3.98 ± 2.81	4.51 ± 2.24	3.25 ± 4.21	3.50 ± 3.91
J1044-5737	1.92 ± 0.85	1.66 ± 3.39	1.81 ± 1.17	1.82 ± 0.75	1.64 ± 2.00	1.70 ± 1.79
J1057-5851	1.79 ± 0.61	0.87 ± 1.81	1.83 ± 1.00	0.73 ± 0.32	0.86 ± 1.02	1.46 ± 1.41
J1105-6037	1.68 ± 0.70	1.66 ± 3.46	1.85 ± 1.12	1.49 ± 0.58	1.63 ± 1.92	1.79 ± 1.80
J1111-6039	6.51 ± 3.10	4.46 ± 8.86	5.07 ± 3.54	6.03 ± 2.79	4.49 ± 5.71	4.63 ± 5.11
J1135-6055	4.37 ± 2.04	3.67 ± 7.42	3.86 ± 2.60	4.40 ± 1.88	3.64 ± 4.50	3.64 ± 3.92
J1139-6247	1.46 ± 0.68	2.51 ± 5.33	1.89 ± 1.17	1.90 ± 0.68	2.51 ± 2.84	2.16 ± 2.16
J1203-6242	4.14 ± 2.00	4.14 ± 8.44	3.87 ± 2.62	4.75 ± 1.95	4.08 ± 5.00	3.84 ± 4.12
J1208-6238	8.51 ± 3.02	1.95 ± 3.78	5.39 ± 3.36	1.17 ± 1.02	2.04 ± 2.70	3.46 ± 3.73
J1231-5113	0.20 ± 0.08	0.69 ± 1.57	0.42 ± 0.22	0.25 ± 0.08	0.85 ± 0.84	0.70 ± 0.61
J1231-6511	2.42 ± 0.96	2.10 ± 4.37	2.64 ± 1.57	1.86 ± 0.73	2.06 ± 2.43	2.46 ± 2.45
J1350-6225	1.38 ± 0.62	1.88 ± 3.96	1.64 ± 1.02	1.58 ± 0.59	1.86 ± 2.15	1.75 ± 1.77
J1358-6025	1.91 ± 1.04	4.28 ± 9.06	2.39 ± 1.61	3.54 ± 1.28	4.25 ± 4.88	2.96 ± 3.08
J1413-6205	1.37 ± 0.65	1.51 ± 3.09	1.37 ± 0.90	1.58 ± 0.62	1.48 ± 1.78	1.39 ± 1.46
J1422-6138	1.56 ± 0.57	0.91 ± 1.87	1.51 ± 0.88	0.87 ± 0.37	0.90 ± 1.08	1.25 ± 1.25
J1429-5911	1.52 ± 0.71	1.70 ± 3.52	1.56 ± 1.02	1.73 ± 0.68	1.67 ± 2.00	1.58 ± 1.65
J1447-5757	1.73 ± 0.75	2.11 ± 4.42	2.01 ± 1.24	1.80 ± 0.68	2.08 ± 2.42	2.07 ± 2.09
J1459-6053	1.68 ± 0.80	1.92 ± 3.94	1.69 ± 1.12	2.01 ± 0.79	1.88 ± 2.26	1.73 ± 1.82
J1522-5735	1.73 ± 0.71	1.30 ± 2.67	1.67 ± 1.04	1.33 ± 0.55	1.28 ± 1.55	1.49 ± 1.54

Table 3.2: *(Continued table from previous page)*

Name	$Dist_P$	$Dist_\tau$	$Dist_{B_{LC}}$	$Dist_{\zeta_1}$	$Dist_{\zeta_2}$	$Dist_{\zeta_3}$
J1528-5838	1.30 ± 0.48	1.05 ± 2.21	1.50 ± 0.85	0.85 ± 0.33	1.04 ± 1.20	1.39 ± 1.34
J1615-5137	1.22 ± 0.52	1.47 ± 3.10	1.46 ± 0.88	1.21 ± 0.45	1.46 ± 1.68	1.50 ± 1.49
J1620-4927	0.64 ± 0.27	0.79 ± 1.66	0.77 ± 0.46	0.65 ± 0.24	0.78 ± 0.90	0.79 ± 0.79
J1623-5005	1.16 ± 0.58	2.18 ± 4.62	1.45 ± 0.94	1.79 ± 0.64	2.17 ± 2.49	1.69 ± 1.73
J1624-4041	0.96 ± 0.41	1.44 ± 3.06	1.26 ± 0.75	1.05 ± 0.37	1.44 ± 1.62	1.39 ± 1.36
J1641-5317	1.11 ± 0.47	1.74 ± 3.74	1.51 ± 0.89	1.21 ± 0.42	1.76 ± 1.97	1.70 ± 1.65
J1650-4601	1.57 ± 0.72	1.92 ± 3.99	1.73 ± 1.10	1.78 ± 0.68	1.88 ± 2.22	1.78 ± 1.83
J1714-3830	3.96 ± 2.00	3.73 ± 7.51	3.43 ± 2.40	4.73 ± 2.02	3.70 ± 4.61	3.40 ± 3.73
J1736-3422	2.20 ± 0.82	1.41 ± 2.92	2.24 ± 1.30	1.29 ± 0.54	1.39 ± 1.66	1.91 ± 1.90
J1742-3321	0.80 ± 0.36	1.72 ± 3.76	1.22 ± 0.72	1.03 ± 0.36	1.80 ± 1.96	1.52 ± 1.46
J1746-3239	0.70 ± 0.29	0.92 ± 1.96	0.90 ± 0.52	0.69 ± 0.24	0.92 ± 1.04	0.95 ± 0.93
J1803-2149	1.68 ± 0.80	2.03 ± 4.19	1.76 ± 1.15	2.03 ± 0.79	1.99 ± 2.37	1.81 ± 1.90
J1813-1246	2.07 ± 1.18	3.21 ± 6.55	2.01 ± 1.46	3.76 ± 1.46	3.15 ± 3.84	2.33 ± 2.56
J1817-1742	2.19 ± 0.97	2.37 ± 4.92	2.36 ± 1.49	2.23 ± 0.87	2.33 ± 2.75	2.34 ± 2.41
J1826-1256	1.88 ± 0.89	1.43 ± 2.87	1.56 ± 1.07	1.83 ± 0.81	1.43 ± 1.79	1.45 ± 1.58
J1827-1446	1.22 ± 0.42	0.77 ± 1.62	1.36 ± 0.74	0.63 ± 0.25	0.76 ± 0.89	1.17 ± 1.12
J1838-0537	5.13 ± 2.28	2.62 ± 5.16	3.72 ± 2.55	3.48 ± 1.78	2.67 ± 3.45	3.11 ± 3.43
J1844-0346	6.22 ± 2.94	4.44 ± 8.87	5.03 ± 3.47	5.78 ± 2.63	4.45 ± 5.62	4.60 ± 5.04
J1846+0919	0.91 ± 0.36	1.05 ± 2.22	1.13 ± 0.66	0.82 ± 0.30	1.05 ± 1.19	1.15 ± 1.12
J1906+0722	2.22 ± 1.05	2.27 ± 4.65	2.15 ± 1.43	2.47 ± 1.00	2.23 ± 2.71	2.13 ± 2.26
J1932+1916	2.23 ± 0.91	1.52 ± 3.09	2.05 ± 1.28	1.61 ± 0.70	1.49 ± 1.83	1.78 ± 1.86
J1954+2836	1.82 ± 0.90	2.24 ± 4.62	1.86 ± 1.24	2.35 ± 0.91	2.20 ± 2.65	1.95 ± 2.06
J1957+5033	0.55 ± 0.20	0.59 ± 1.28	0.75 ± 0.40	0.40 ± 0.14	0.60 ± 0.67	0.78 ± 0.73
J1958+2846	1.91 ± 0.72	0.97 ± 1.95	1.64 ± 1.00	1.02 ± 0.48	0.96 ± 1.19	1.31 ± 1.35
J2017+3625	0.31 ± 0.13	0.64 ± 1.39	0.48 ± 0.28	0.38 ± 0.13	0.67 ± 0.72	0.60 ± 0.56
J2028+3332	0.64 ± 0.27	0.94 ± 2.01	0.84 ± 0.50	0.68 ± 0.24	0.95 ± 1.06	0.93 ± 0.90
J2055+2539	0.34 ± 0.13	0.44 ± 0.96	0.49 ± 0.27	0.28 ± 0.10	0.46 ± 0.50	0.54 ± 0.50
J2111+4606	4.46 ± 1.93	2.86 ± 5.74	3.72 ± 2.44	3.44 ± 1.56	2.85 ± 3.57	3.23 ± 3.46

Table 3.2: *(Continued table from previous page)*

Name	$Dist_P$	$Dist_\tau$	$Dist_{B_{LC}}$	$Dist_{\zeta_1}$	$Dist_{\zeta_2}$	$Dist_{\zeta_3}$
J2139+4716	0.36 ± 0.14	0.59 ± 1.28	0.56 ± 0.30	0.33 ± 0.11	0.62 ± 0.66	0.68 ± 0.62
J2238+5903	2.87 ± 1.23	2.07 ± 4.19	2.56 ± 1.65	2.34 ± 1.01	2.05 ± 2.52	2.28 ± 2.41

When we examine the overall results of Wang's Approach, we see mixed outcomes. On one hand, we have outlier predictions with up to 1300% error, inadequate linear fits that do not seem to represent most of the data, and relatively low R^2_{adj} values around 0.25, meaning that only 25 percent of the variations seen in the data can be explained. On the other hand, we observe a promising distribution of relative errors and residuals with reasonable mean, median and standard deviation values. This leads us to conclude that linear regression using a single variable is not a reliable method for accurately estimating the distance values of radio-quiet pulsars and can only be used as a rough estimation.

Apart from the results, when we look at the core scientific assumptions of this approach, we see parameters that depend on somewhat outdated models, such as the polar cap model. Using such a model while trying to estimate the distance values of radio-quiet pulsars seems rather troublesome, considering the polar cap model cannot explain the existence of such pulsars. In the end, we are left with a statistical approach that is not based on a reliable scientific foundation and yields somewhat mixed results. For these reasons, we cannot be confident in our results from Wang's Approach.

CHAPTER 4

RESULTS AND DISCUSSION FOR FUNDAMENTAL PLANE APPROACH

The constants of the fits of equations FP-1, FP-2, and FP-3, alongside R^2_{adj} values of the fits, are given in Table 4.1. We can immediately see the improvements in R^2_{adj} values over Wang's Approach. As expected, separating the data into millisecond and young groups showed a decrease in R^2_{adj}, caused by the reduction in data points. However, the difference does not seem to be as impactful as Wang's Approach claims. In both our analysis and the Fundamental Plane Approach, both millisecond and young pulsars seem to obey the Fundamental Plane relation (Eqs. 1.2, 1.4, and 1.8) proposed by Kalapotharakos et al. (2022). This implies that the Fundamental Plane Approach does not need to separate data into millisecond and young pulsar groups like we did in Wang's Approach.

[t]

Table 4.1: Fit results for equations FP-1 (Eq. 2.3), FP-2 (Eq. 2.4) and FP-3 (Eq. 2.5). The numbers in parenthesis are their relative error given in units of standard deviation (sigma) compared to theoretical exponential values in Eqs. 1.2, 1.4 and 1.8.

Fit	Constant a	constant b	Constant c	Constant d	R^2_{adj}
All FP-1	17.6 ± 1.57	$1.26 \pm 0.15(0.50)$	$0.12 \pm 0.033(1.65)$	$0.42 \pm 0.05(0.00)$	0.74
All FP-2	15.5 ± 1.50	$2.03 \pm 0.27(2.60)$	$0.13 \pm 0.03(1.35)$	$0.49 \pm 0.05(1.52)$	0.73
All FP-3	39.4 ± 0.48	$1.26 \pm 0.15(0.50)$	$-1.19 \pm 0.17(0.13)$	$0.48 \pm 0.04(0.52)$	0.74
Young FP-1	20.7 ± 3.01	$1.31 \pm 0.26(0.08)$	$-0.05 \pm 0.18(1.16)$	$0.39 \pm 0.08(0.36)$	0.64
Young FP-2	17.1 ± 2.66	$1.90 \pm 0.36(1.60)$	$0.13 \pm 0.19(0.18)$	$0.44 \pm 0.07(0.36)$	0.65
Young FP-3	37.9 ± 1.37	$1.31 \pm 0.26(0.08)$	$-1.19 \pm 0.29(0.07)$	$0.36 \pm 0.10(1.34)$	0.64
MS FP-1	15.4 ± 2.34	$1.24 \pm 0.19(0.49)$	$0.046 \pm 0.15(0.79)$	$0.50 \pm 0.08(1.11)$	0.57
MS FP-2	12.7 ± 2.33	$3.06 \pm 0.53(3.29)$	$-0.05 \pm 0.16(1.38)$	$0.62 \pm 0.07(2.71)$	0.53
MS FP-3	39.6 ± 1.61	$1.24 \pm 0.16(0.49)$	$-1.48 \pm 0.26(1.17)$	$0.52 \pm 0.08(0.27)$	0.57

After plotting ϵ_{cut}, B_*, and $\dot{E}$ against luminosity in 4.1, we can also see a clear divide in their surface magnetic fields, with millisecond pulsars generally having weaker magnetospheres. If we recall the outer-gap model from Chapter 1, their weaker magnetic fields mean that the sources of gamma and radio emissions are much closer to each other and have a wider range due to the larger curvature of their magnetic field lines. This explains why only five of the radio-quiet pulsars are millisecond pulsars, while they are abundant among radio-emitting pulsars.

We can also note that millisecond pulsars generally have lower luminosity values. Although this can be attributed to millisecond pulsars having intrinsically lower luminosities compared to their counterparts, which creates an observational bias where we can only detect the closer millisecond pulsars, it does not fully explain why there are more millisecond pulsar discoveries than young pulsars. When examining the dis-

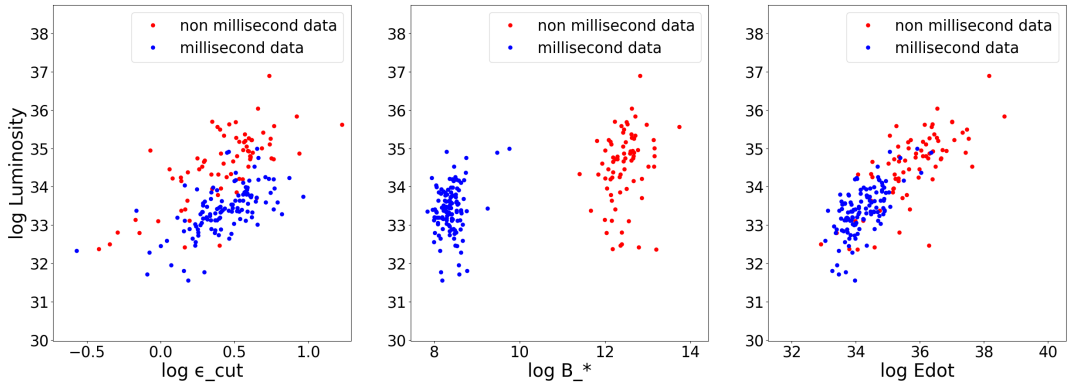


Figure 4.1: Distribution of variables used in FP with respect to luminosity. One can note the obvious grouping.

tance data, we find that the average distance of 125 millisecond pulsars is 1.94 kpc, whereas the average distance of 75 young pulsars is 4.01 kpc. However, this is not surprising and can be explained as Lorimer and Kramer (2004) describes in his book: the long lifetimes of millisecond pulsars mean that they are more likely to be found in our local region of the galaxy, where many such systems have had time to evolve. Young pulsars, on the other hand, are often found in or near their birthplaces, such as supernova remnants, which can be located farther from us and spread across the galaxy.

To evaluate the success of our fits, we substituted the constants from Table 4.1 back into the FP-1, FP-2, and FP-3 equations using the 195 pulsars to obtain predicted distance values, which are shown in Fig. 4.2. Since the x and y axes are the same as in Fig. 3.1, we can immediately notice that the distribution around the $x = y$ line is much stronger. Although we have more data points, we still do not see substantial agreement between our predictions and any particular distance measurement methods from Fermi 3PC. Additionally, it is worth noting that the first and third plots are identical. This is because FP-3 is simply a derivation of FP-1, and despite having different fit parameters, it yields almost identical (agreeing up to 6 significant figures) predicted distance values. Since we confirmed that the FP-3 relation is just a derivation of FP-1 and provides the same distance and luminosity predictions, we will focus on FP-1 and FP-2 from now on.

We also created histograms showing the distribution of relative errors and residuals

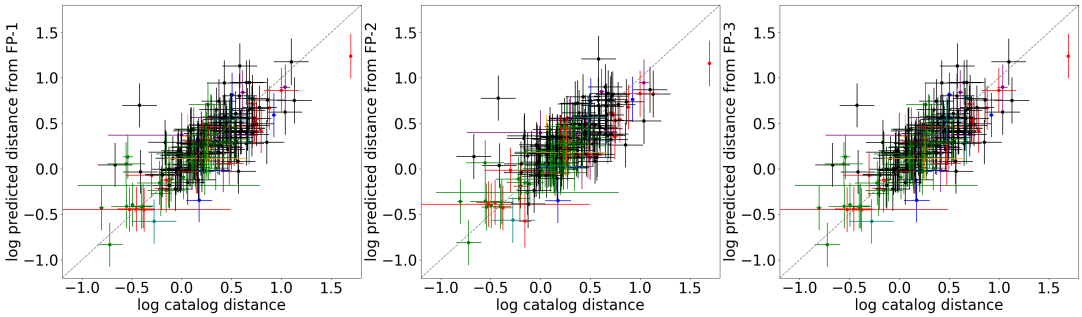


Figure 4.2: Fermi 3PC distance values versus predicted distance values using FP-1, FP-2, and FP-3 in logarithmic form. The color scheme is the same as in Fig. 3.1, and the gray dashed line represents the $x = y$ line to illustrate the distribution of the data.

of distance predictions, which can be seen in Fig. 4.3. In upper panel of Fig. 4.3, we observe that one pulsar in particular (J0940-5428) exhibits relative error value up to 14 times, indicating it either over-predicts or under-predicts (since the histogram shows relative error in absolute value) the catalog distance by a factor of 14. We believe this outlier is due to the pulsar having only 3 observed points on its SED, which may have led to inaccurate calculations of ϵ_{cut} and ϵ_{10}. Despite this outlier, the median relative error is around 0.3, suggesting that 50% of our predictions have a relative error less than 0.3. Although the negative mean in Fig. **??** suggests that our predictions are slightly under-predicting the distance values (the means are -0.06 and -0.07 without the outlier pulsar J0540-6919), we observe a Gaussian distribution around 0, with a standard deviation around 3, indicating promising results.

In order to verify the success of our fits, we employed the "Group A" and "Group B" method. By calculating the constants from "Group A" and obtaining distance predictions for "Group B," we created 100 histograms for FP-1 and FP-2 relations, similar to Fig. 4.3. We then compiled the means of relative errors and medians of residues into histograms, shown in Fig. 4.4. The results indicate that for most "Group A" and "Group B" separations, the means of residues and medians of relative errors fall within a reasonable range, with a slight under-prediction bias in some cases. This "independent" approach corroborates our previous findings and strengthens our confidence in the success of the Fundamental Plane Approach.

One should note that during this analysis, we excluded the outlier pulsar J0940-5428,

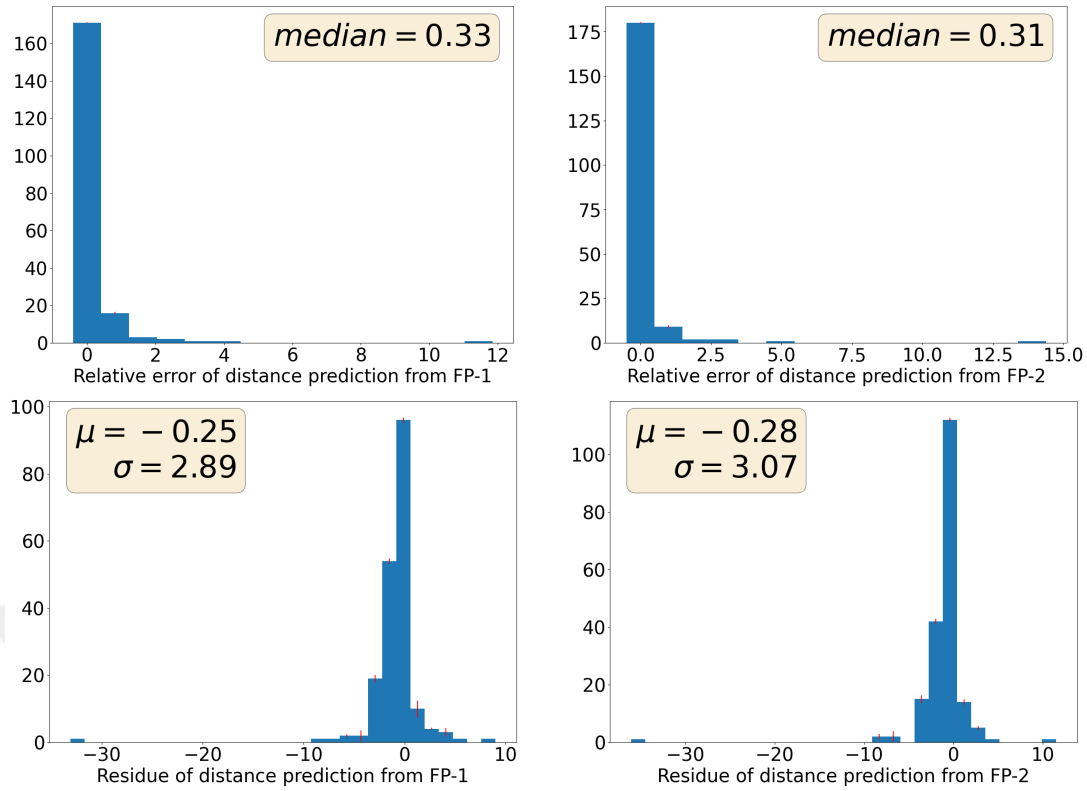


Figure 4.3: In the top panel, we present 15-bin histograms of the relative errors of predicted distances using FP-1 and FP-2, with median values indicated in the top right corner. The bottom panel displays 30-bin histograms of the residuals of predicted distances using FP-1 and FP-2, with mean and standard deviation values shown in the top left corner. Error bars are represented by vertical red lines.

which can be seen in Fig. 4.3 on the right-hand side of the histogram. This pulsar had such a strong effect on the analysis that, when it was included in "Group B," it would heavily skew the mean to much higher values and create two peaks in the histograms.

Finally, the original aim of this study, the distance estimations of 62 radio-quiet pulsars using the FP-1 and FP-2 equations can be seen in Table 4.2. It is worth noting that there is an upper limit to the distance for radio-quiet pulsars in the Fermi Catalog. However, these limits are upper 95% limits (Smith et al., 2023) and do not provide relevant information about the success of our distance estimations, as all of our estimations are below these limits.

After analyzing the R^2_{adj} values, relative errors, and residuals, we can conclude that

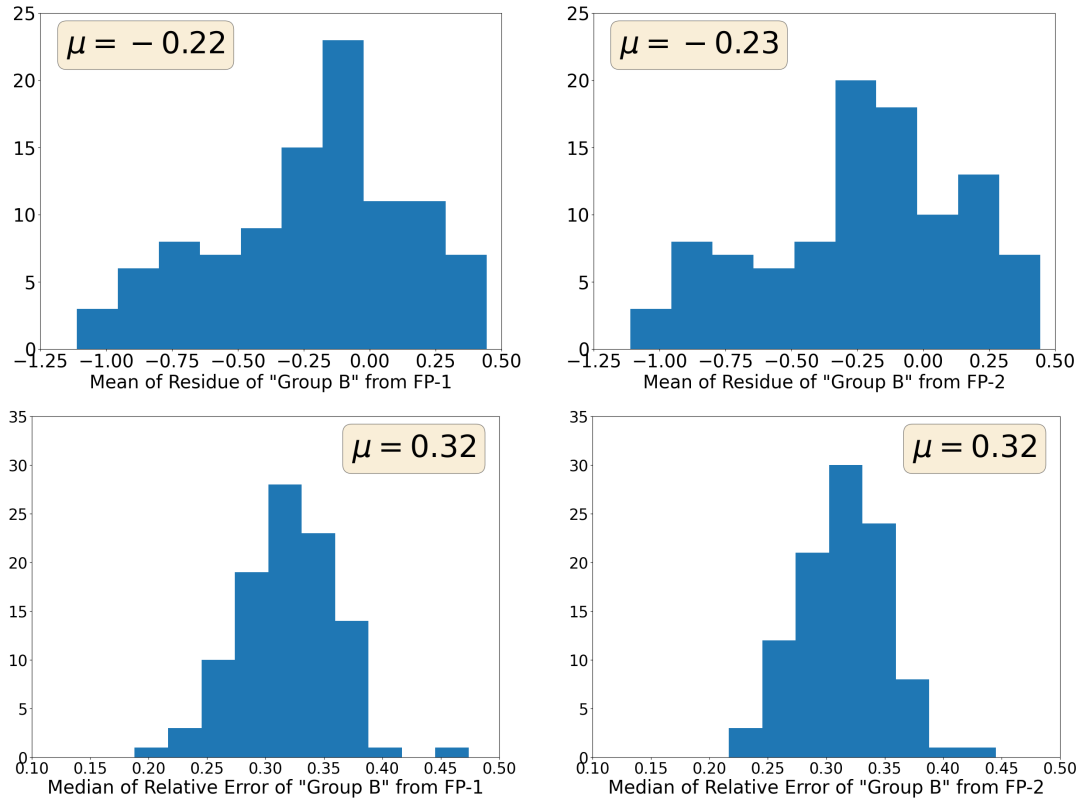


Figure 4.4: Histograms of the mean values of residues and median value of relative errors from 100 different "Group B" pulsar sets using FP-1 and FP-2. These histograms use 10 bins, and the mean of the data is given in the upper corners.

the Fundamental Plane Approach is more promising than Wang's Approach. This is due to its stronger scientific foundation and more successful predictions.

Table 4.2: Calculated distance values of 62 pulsars using FP-1 and FP-2.

PSRJ	Distance from FP-1 (kpc)	Distance from FP-2 (kpc)
J0357+3205	0.521 ± 0.278	0.546 ± 0.295
J0359+5414	4.264 ± 2.237	5.186 ± 2.759
J0554+3107	1.951 ± 1.031	2.321 ± 1.246
J0622+3749	1.081 ± 0.573	1.239 ± 0.665
J0633+0632	1.478 ± 0.779	1.603 ± 0.859
J0734-1559	2.270 ± 1.193	2.015 ± 1.074
J0744-2525	2.051 ± 1.076	2.223 ± 1.185
J0802-5613	1.561 ± 0.831	1.789 ± 0.968
J1023-5746	3.451 ± 1.822	3.635 ± 1.948
J1044-5737	2.116 ± 1.108	2.042 ± 1.086
J1057-5851	1.368 ± 0.732	1.716 ± 0.932
J1105-6037	2.523 ± 1.334	2.536 ± 1.361
J1111-6039	5.414 ± 2.850	7.371 ± 3.953
J1135-6055	4.385 ± 2.301	4.557 ± 2.428
J1139-6247	4.254 ± 2.265	3.756 ± 2.023
J1203-6242	4.691 ± 2.468	4.872 ± 2.603
J1208-6238	7.031 ± 3.743	6.534 ± 3.526
J1231-5113	0.518 ± 0.278	0.463 ± 0.252
J1231-6511	2.728 ± 1.442	2.950 ± 1.583
J1335-5656	1.969 ± 1.034	1.859 ± 0.990

Table 4.2: *(Continued table from previous page)*

PSRJ	Distance from FP-1 (kpc)	Distance from FP-2 (kpc)
J1350-6225	2.444 ± 1.290	2.630 ± 1.412
J1358-6025	3.513 ± 1.847	3.294 ± 1.757
J1413-6205	1.775 ± 0.930	2.057 ± 1.097
J1422-6138	2.011 ± 1.063	2.511 ± 1.356
J1429-5911	1.999 ± 1.047	1.841 ± 0.979
J1447-5757	1.954 ± 1.029	1.785 ± 0.955
J1459-6053	2.170 ± 1.137	1.905 ± 1.012
J1522-5735	1.862 ± 0.977	1.917 ± 1.022
J1528-5838	1.959 ± 1.042	2.179 ± 1.179
J1615-5137	1.742 ± 0.917	2.287 ± 1.228
J1620-4927	1.307 ± 0.690	1.316 ± 0.706
J1623-5005	2.187 ± 1.148	2.870 ± 1.538
J1624-4041	1.707 ± 0.898	1.790 ± 0.957
J1641-5317	1.794 ± 0.946	1.919 ± 1.027
J1649-3012	1.440 ± 0.754	1.473 ± 0.783
J1650-4601	2.124 ± 1.117	2.302 ± 1.230
J1714-3830	4.383 ± 2.313	5.361 ± 2.881
J1736-3422	2.868 ± 1.531	3.177 ± 1.726
J1742-3321	1.656 ± 0.884	1.926 ± 1.045
J1744-7619	0.590 ± 0.309	0.650 ± 0.345

Table 4.2: *(Continued table from previous page)*

PSRJ	Distance from FP-1 (kpc)	Distance from FP-2 (kpc)
J1746-3239	1.218 ± 0.642	1.297 ± 0.695
J1803-2149	2.524 ± 1.326	2.754 ± 1.472
J1813-1246	1.999 ± 1.051	1.974 ± 1.054
J1817-1742	3.923 ± 2.088	3.618 ± 1.951
J1826-1256	1.612 ± 0.846	1.696 ± 0.904
J1827-0849	2.350 ± 1.253	1.393 ± 0.745
J1827-1446	0.999 ± 0.532	1.641 ± 0.889
J1838-0537	3.629 ± 1.916	4.595 ± 2.468
J1844-0346	3.760 ± 1.989	5.098 ± 2.732
J1846+0919	1.489 ± 0.785	1.683 ± 0.903
J1906+0722	2.968 ± 1.562	2.695 ± 1.438
J1932+1916	2.092 ± 1.099	2.118 ± 1.129
J1954+2836	2.344 ± 1.228	2.610 ± 1.389
J1957+5033	0.780 ± 0.415	0.745 ± 0.402
J1958+2846	1.714 ± 0.901	1.963 ± 1.048
J2017+3625	0.707 ± 0.374	0.686 ± 0.368
J2028+3332	0.906 ± 0.476	1.174 ± 0.627
J2034+3632	0.597 ± 0.313	0.716 ± 0.382
J2055+2539	0.586 ± 0.312	0.647 ± 0.349
J2111+4606	4.940 ± 2.597	4.911 ± 2.622

Table 4.2: *(Continued table from previous page)*

PSRJ	Distance from FP-1 (kpc)	Distance from FP-2 (kpc)
J2139+4716	0.600 ± 0.319	0.681 ± 0.368
J2238+5903	3.029 ± 1.589	2.975 ± 1.584

CHAPTER 5

CONCLUSIONS

If we examine and compare the overall results obtained from Wang's Approach, a few conclusions can be drawn. Firstly, the linear fit used in Wang's Approach was inadequate for highlighting a significant linear relationship between gamma-ray emission efficiency and the six parameters analyzed. This suggests either the linear fit is too simplistic and a more complex relationship exists, or no such relationship correlating gamma-ray emission efficiency with these six parameters exists. Since Wang's Approach does not consider potential physical processes that might create such a relationship, and given the presence of many outlier data points in the distributions shown in Fig. 2.2 that do not conform to a linear relationship, we lean towards the latter conclusion.

Secondly, the use of generation order parameters (ζ_1, ζ_2, ζ_3) based on the polar-cap model to predict the distances of radio-quiet pulsars undermines the scientific basis of this approach. Thirdly, in the linear fits we utilized, both x variables (period P, characteristic age τ, magnetic field at light cylinder B_{LC}, and generation order parameters) and the y variable (gamma-ray emission efficiency η) were dependent on the period and its derivative. This interdependence between x and y variables reduces the credibility of the linear fits. Additionally, excluding all millisecond pulsars due to their differing physical properties significantly limits the number of usable data points. For these reasons, we conclude that Wang's Approach is not suitable for precise distance predictions of radio-quiet pulsars.

On the other hand, analyzing the results from the Fundamental Plane Approach reveals that the proposed theoretical relation is consistent with the observational data and is grounded in a more robust scientific framework. Additionally, our distance

predictions for 62 radio-quiet pulsars fall within an acceptable precision range. However, due to the exponential nature of the linear fit constants, even small errors in the linear fits translate into substantial error bars in our distance predictions. This situation highlights the need for more precise fitting algorithms, such as random forest regression or support vector machines, in future studies.

Moreover, the significant increase in the number of gamma-ray pulsar discoveries—from 46 in 2010 (Abdo et al., 2010) to 294 in 2023 (Smith et al., 2023) suggests that future discoveries will further reduce the error in our distance predictions, leading to more accurate results.

In conclusion, the Fundamental Plane relation proposed by Kalapotharakos et al. (2022) can, in principle, be used to predict distances for radio-quiet gamma-ray pulsars and provides promising results with reasonable error margins. These results can be improved upon with further studies and increased data.

REFERENCES

Abdo, A. A., Ackermann, M., Ajello, M., Atwood, W. B., Axelsson, M., Baldini, L., Ballet, J., Barbiellini, G., Baring, M. G., Bastieri, D., Baughman, B. M., Bechtol, K., Bellazzini, R., Berenji, B., Blandford, R. D., Bloom, E. D., Bonamente, E., Borgland, A. W., Bregeon, J., ..., and Ziegler, M. (2010). The First Fermi Large Area Telescope Catalog of Gamma-ray Pulsars. , 187(2):460–494.

Abdo, A. A., Ajello, M., Allafort, A., Baldini, L., Ballet, J., Barbiellini, G., Bastieri, D., Bellazzini, R., Berenji, B., Blandford, R. D., Bloom, E. D., Bonamente, E., Borgland, A. W., Bottacini, E., Brandt, T. J., Bregeon, J., Brigida, M., Bruel, P., Buehler, R., Buson, S., Caliandro, G. A., Cameron, R. A., Caraveo, P. A., Cecchi, C., and ... (2013). The second fermi large area telescope catalog of gamma-ray pulsars. *The Astrophysical Journal Supplement Series*, 208(2):17.

Adelsberg, E. V., Will, C. M., and Doran, J. E. K. (2017). A population of millisecond pulsars in the galactic halo. *Nature Astronomy*, 1:256–259.

Aliu, E., H, A., Antonelli, L. A., Antoranz, P., Backes, M., C, B., Barrio, J. A., Bartko, H., Bastieri, D., JK, B., W, B., Berger, K., E, B., Bigongiari, C., A, B., RK, B., Bonnoli, G., Bordas, P., V, B.-R., and ED, W. (2008). Observation of pulsed gamma-rays above 25 gev from the crab pulsar with magic. *SCIENCE*, 322:1221–1224.

Arons, J. (2019). The polar-cap and outer-cap models of pulsar emission. *Annual Review of Astronomy and Astrophysics*, 57:185–220.

Australia Telescope National Facility (2024). Atnf pulsar catalog. Accessed: 2024-08-07.

Becker, W. and Truemper, J. (1997). The X-ray luminosity of rotation-powered neutron stars. , 326:682–691.

Cheng, K. S., Taam, R. E., and Wang, W. (2004). Pulsar Wind Nebulae and the X-Ray Emission of Nonaccreting Neutron Stars. , 617(1):480–489.

Cordes, J. M. and Lazio, T. J. W. (2002). Ne2001. i. a new model for the galactic distribution of free electrons. *The Astrophysical Journal*, 575(1):453–470.

Hardcastle, M. J., Lyne, A. G., and Lorimer, D. R. (1995). The outer gap model of pulsar emission. *Monthly Notices of the Royal Astronomical Society*, 273:163–168.

Hewish, A., Bell, S. J., Pilkington, J. D. H., Scott, P. F., and Collins, R. A. (1968). Observation of a Rapidly Pulsating Radio Source. , 217(5130):709–713.

Johnston, S. and Bailes, M. (2018). *Pulsar Astronomy: The State of the Art*. Cambridge University Press.

Kalapotharakos, C., Harding, A. K., Kazanas, D., and Wadiasingh, Z. (2019). A Fundamental Plane for Gamma-Ray Pulsars. , 883(1):L4.

Kalapotharakos, C., Wadiasingh, Z., Harding, A. K., and Kazanas, D. (2022). The Fundamental Plane Relation for Gamma-Ray Pulsars Implied by 4FGL. , 934(1):65.

Kramer, M., Pooley, J. H. T., and Kramer, M. D. (2016). Millisecond pulsars and their evolution. *Annual Review of Astronomy and Astrophysics*, 54:281–318.

Kramer, M. and Wex, N. (2020). *The Physics of Pulsars*. Springer.

Longo, M. and et al., R. S. S. (2011). *Gamma-Ray Astronomy*. Springer.

Lorimer, D. R. and Kramer, M. (2004). *Handbook of Pulsar Astronomy*. Cambridge University Press, Cambridge, UK.

Manchester, R. N. (2017). The detection of fast radio bursts. *Proceedings of the International Astronomical Union*, 13(S337):109–115.

Montgomery, D. C., Peck, E. A., and Vining, G. G. (2012). *Introduction to Linear Regression Analysis*. Wiley, Hoboken, NJ, 5th edition.

Saito, Y. (1998). Discovery of the non-thermal X-ray pulsation from the millisecond pulsar PSR B1821-24. *Astronomical Herald*, 91(8):346–351.

Seabold, S. and Perktold, J. (2010). statsmodels: Econometric and statistical modeling with python. In *9th Python in Science Conference*.

Shklovskii, I. S. (1970). On the nature of pulsar period changes. *Soviet Astronomy*, 13:562–569.

Smith, D. A., Abdollahi, S., Ajello, M., Bailes, M., Baldini, L., Ballet, J., Baring, M. G., Bassa, C., Gonzalez, J. B., Bellazzini, R., Berretta, A., Bhattacharyya, B., Bissaldi, E., Bonino, R., Bottacini, E., Bregeon, J., Bruel, P., Burgay, M., Burnett, T. H., ..., and Zhu, W. (2023). The Third Fermi Large Area Telescope Catalog of Gamma-Ray Pulsars. , 958(2):191.

Sturrock, P. A. (1983). A model of pulsar magnetospheres. *Astrophysical Journal*, 274:333–341.

Taylor, J. H. and Manchester, J. M. (2016). Pulsar ages and spin-down models. *Physics Reports*, 586:1–45.

Thompson, D. J. (2001). Gamma-ray pulsars: Multiwavelength observations. *The Astrophysical Journal Supplement Series*, 120(2):495–499.

Thompson, D. J., Bailes, M., Bertsch, D. L., Cordes, J., D'Amico, N., Esposito, J. A., Finley, J., Hartman, R. C., Hermsen, W., Kanbach, G., Kaspi, V. M., Kniffen, D. A., Kuiper, L., Lin, Y. C., Lyne, A., Manchester, R., Matz, S. M., Mayer-Hasselwander, H. A., Michelson, P. F., ..., and Ulmer, M. (1999). Gamma Radiation from PSR B1055-52. , 516(1):297–306.

Verbiest, J. P. W., Weisberg, J. M., Chael, A. A., Lee, K. J., and Lorimer, D. R. (2012). On Pulsar Distance Measurements and Their Uncertainties. , 755(1):39.

Wang, W. (2011). Possible distance indicators in gamma-ray pulsars. *Research in Astronomy and Astrophysics*, 11(7):824–832.

Watters, K. P., Romani, R. W., Weltevrede, P., and Johnston, S. (2009). An Atlas for Interpreting γ-Ray Pulsar Light Curves. , 695(2):1289–1301.

Weinberg, S. (2008). *Cosmology*. Oxford University Press.

Wooldridge, J. M. (2016). *Introductory Econometrics: A Modern Approach*. Cengage Learning, Boston, MA, 6th edition.

Yao, J. M., Manchester, R. N., and Wang, N. (2016). A new electron density model for the galactic thin disk. *The Astrophysical Journal*, 832(1):204.

APPENDIX

A Table of Pulsars Used in Analysis

Table A.1: 195 pulsars with known distance values and their relevant parameters used in this study.

PSRJ	Period	$\dot{P}$	$\dot{E}$	B_{Star}	D3PC	Flux	Luminosity	e_{cut}	e_{10}
J0002+6216	1.15E-01	5.97E-15	1.53E+35	8.40E+11	2.00E+00	1.88E-11	9.01E+33	2.55E+00	9.25E-01
J0007+7303	3.16E-01	3.56E-13	4.46E+35	1.07E+13	1.40E+00	4.32E-10	1.01E+35	4.83E+00	1.39E+00
J0023+0923	3.05E-03	8.88E-21	1.24E+34	1.84E+08	1.80E+00	7.83E-12	3.03E+33	2.54E+00	1.00E+00
J0030+0451	4.87E-03	1.05E-20	3.60E+33	2.25E+08	3.20E-01	6.04E-11	7.43E+32	2.34E+00	1.00E+00
J0034-0534	1.88E-03	4.47E-21	2.66E+34	9.79E+07	1.35E+00	2.02E-11	4.38E+33	3.62E+00	1.09E+00
J0101-6422	2.57E-03	3.44E-21	8.01E+33	1.12E+08	1.00E+00	1.30E-11	1.56E+33	2.52E+00	1.03E+00
J0102+4839	2.96E-03	1.16E-20	1.76E+34	1.88E+08	2.31E+00	1.50E-11	9.59E+33	3.87E+00	1.25E+00
J0106+4855	8.32E-02	4.28E-16	2.94E+34	1.91E+11	3.06E+00	1.92E-11	2.16E+34	2.99E+00	1.13E+00
J0205+6449	6.57E-02	1.92E-13	2.67E+37	3.60E+12	3.20E+00	6.43E-11	7.88E+34	4.19E+00	8.85E-01
J0218+4232	2.32E-03	7.65E-20	2.42E+35	4.29E+08	3.15E+00	4.83E-11	5.74E+34	4.57E+00	1.04E+00
J0248+4230	2.60E-03	1.68E-20	3.78E+34	2.12E+08	1.85E+00	1.94E-12	7.95E+32	1.56E+00	9.28E-01
J0248+6021	2.17E-01	5.52E-14	2.13E+35	3.50E+12	2.00E+00	2.94E-11	1.41E+34	1.38E+00	7.53E-01
J0251+2606	2.54E-03	5.29E-21	1.28E+34	1.40E+08	1.17E+00	4.88E-12	7.99E+32	2.20E+00	9.97E-01
J0307+7443	3.16E-03	1.71E-20	2.17E+34	2.35E+08	3.86E-01	1.64E-11	2.93E+32	1.71E+00	9.29E-01
J0312-0921	3.70E-03	1.25E-20	9.70E+33	2.73E+08	8.17E-01	5.54E-12	4.43E+32	1.64E+00	9.02E-01
J0318+0253	5.19E-03	1.76E-20	4.98E+33	3.06E+08	1.33E+00	6.32E-12	1.33E+33	2.19E+00	1.04E+00
J0340+4130	3.30E-03	5.53E-21	6.08E+33	1.41E+08	1.60E+00	1.93E-11	5.94E+33	3.35E+00	1.30E+00
J0418+6635	2.91E-03	1.37E-20	2.19E+34	2.02E+08	2.21E+00	1.03E-11	6.02E+33	4.11E+00	1.27E+00
J0437-4715	5.76E-03	1.40E-20	2.89E+33	5.81E+08	1.57E-01	1.76E-11	5.17E+31	8.08E-01	6.29E-01
J0514-4408	3.20E-01	2.04E-15	2.45E+33	8.18E+11	9.66E-01	5.58E-12	6.23E+32	7.16E-01	4.82E-01
J0533+6759	4.39E-03	1.26E-20	5.90E+33	2.38E+08	2.39E+00	9.32E-12	6.38E+33	3.62E+00	1.22E+00
J0534+2200	3.37E-02	4.20E-13	4.35E+38	3.80E+12	1.96E+00	1.49E-09	6.85E+35	8.32E+00	1.25E+00
J0540-6919	5.06E-02	4.79E-13	1.46E+38	4.98E+12	4.97E+01	2.67E-11	7.89E+36	5.43E+00	9.52E-01
J0605+3757	2.73E-03	4.72E-21	9.17E+33	1.15E+08	2.15E-01	6.44E-12	3.56E+31	1.53E+00	9.43E-01
J0610-2100	3.86E-03	5.10E-21	3.50E+33	2.21E+08	2.20E+00	7.23E-12	4.19E+33	1.98E+00	9.30E-01
J0613-0200	3.06E-03	8.88E-21	1.22E+34	1.73E+08	7.80E-01	3.82E-11	2.78E+33	3.06E+00	1.04E+00

Table A.1: *(Continued table from previous page)*

PSRJ	Period	$\dot{P}$	$\dot{E}$	B_{Star}	D3PC	Flux	Luminosity	e_{cut}	e_{10}
J0614-3329	3.15E-03	1.80E-20	2.27E+34	2.40E+08	6.30E-01	1.15E-10	5.44E+33	4.10E+00	1.43E+00
J0621+2514	2.72E-03	2.49E-20	4.87E+34	2.63E+08	1.64E+00	4.08E-12	1.31E+33	1.45E+00	1.01E+00
J0631+0646	1.11E-01	3.62E-15	1.04E+35	6.41E+11	4.58E+00	1.60E-11	4.03E+34	2.66E+00	1.17E+00
J0631+1036	2.88E-01	1.03E-13	1.70E+35	5.50E+12	2.11E+00	3.03E-11	1.61E+34	3.41E+00	1.12E+00
J0633+1746	2.37E-01	1.10E-14	3.25E+34	1.63E+12	1.90E-01	4.22E-09	1.82E+34	2.79E+00	1.08E+00
J0653+4706	4.75E-03	2.08E-20	7.61E+33	3.18E+08	9.13E-01	1.96E-12	1.95E+32	8.38E-01	6.91E-01
J0659+1414	3.85E-01	5.50E-14	3.80E+34	4.65E+12	2.88E-01	2.65E-11	2.64E+32	1.45E+00	1.95E-01
J0729-1448	2.52E-01	1.13E-13	2.81E+35	5.40E+12	2.68E+00	6.00E-12	5.16E+33	4.45E+00	8.94E-01
J0740+6620	2.88E-03	3.70E-21	6.12E+33	1.90E+08	1.15E+00	2.83E-12	4.48E+32	2.91E+00	1.13E+00
J0742-2822	1.67E-01	1.67E-14	1.42E+35	1.69E+12	2.00E+00	1.52E-11	7.28E+33	3.26E+00	1.04E+00
J0751+1807	3.48E-03	5.93E-21	5.56E+33	1.67E+08	1.11E+00	1.01E-11	1.48E+33	1.93E+00	1.08E+00
J0835-4510	8.94E-02	1.22E-13	6.76E+36	3.35E+12	2.80E-01	9.29E-09	8.72E+34	3.90E+00	1.18E+00
J0908-4913	1.07E-01	1.51E-14	4.90E+35	1.29E+12	1.00E+00	2.19E-11	2.62E+33	1.46E+00	6.61E-01
J0931-1902	4.64E-03	3.32E-21	1.31E+33	1.31E+08	3.72E+00	1.44E-12	2.39E+33	6.80E-01	7.60E-01
J0940-5428	8.76E-02	3.28E-14	1.93E+36	1.71E+12	3.77E-01	1.75E-11	2.97E+32	2.50E+00	9.88E-01
J0952-0607	1.41E-03	4.76E-21	6.65E+34	8.29E+07	6.26E+00	2.36E-12	1.10E+34	1.46E+00	9.14E-01
J0955-6150	1.99E-03	1.46E-20	7.33E+34	1.70E+08	2.17E+00	7.73E-12	4.36E+33	3.42E+00	1.03E+00
J1016-5857	1.07E-01	8.04E-14	2.56E+36	2.97E+12	3.16E+00	7.00E-11	8.38E+34	3.94E+00	1.14E+00
J1019-5749	1.63E-01	2.01E-14	1.85E+35	1.83E+12	1.09E+01	2.72E-11	3.88E+35	5.85E+00	1.22E+00
J1023+0038	1.69E-03	5.23E-21	4.28E+34	1.09E+08	1.37E+00	3.24E-11	7.25E+33	3.69E+00	1.02E+00
J1024-0719	5.16E-03	1.86E-20	5.33E+33	3.13E+08	1.22E+00	4.31E-12	7.67E+32	2.56E+00	1.06E+00
J1028-5819	9.14E-02	1.42E-14	7.34E+35	1.15E+12	1.42E+00	2.45E-10	5.94E+34	4.05E+00	1.21E+00
J1035-6720	2.87E-03	4.56E-20	7.62E+34	3.69E+08	1.46E+00	1.88E-11	4.81E+33	2.18E+00	1.03E+00
J1036-8317	3.41E-03	2.90E-20	2.88E+34	3.27E+08	2.16E+00	4.11E-12	2.29E+33	2.57E+00	1.12E+00
J1048+2339	4.67E-03	2.51E-20	9.73E+33	3.79E+08	1.32E+00	4.90E-12	1.02E+33	4.52E+00	1.16E+00
J1048-5832	1.24E-01	9.55E-14	1.99E+36	3.48E+12	2.90E+00	1.85E-10	1.86E+35	3.95E+00	1.18E+00
J1055-6028	9.97E-02	1.09E-12	4.33E+37	1.05E+13	3.83E+00	1.91E-11	3.36E+34	3.91E+00	1.15E+00
J1057-5226	1.97E-01	5.84E-15	3.01E+34	1.09E+12	3.50E-01	2.96E-10	4.34E+33	1.51E+00	8.32E-01

Table A.1: *(Continued table from previous page)*

PSRJ	Period	$\dot{P}$	$\dot{E}$	B_{Star}	D3PC	Flux	Luminosity	e_{cut}	e_{10}
J1105-6107	6.32E-02	1.58E-14	2.48E+36	1.01E+12	2.36E+00	2.35E-11	1.56E+34	3.60E+00	9.82E-01
J1112-6103	6.50E-02	3.15E-14	4.54E+36	1.45E+12	4.46E+00	2.24E-11	5.33E+34	5.81E+00	1.21E+00
J1119-6127	4.09E-01	4.04E-12	2.33E+36	4.12E+13	8.40E+00	4.40E-11	3.71E+35	2.42E+00	1.18E+00
J1124-3653	2.41E-03	5.91E-21	1.67E+34	1.19E+08	9.90E-01	1.25E-11	1.46E+33	3.45E+00	1.15E+00
J1124-5916	1.36E-01	7.51E-13	1.19E+37	1.02E+13	4.80E+00	6.11E-11	1.68E+35	4.14E+00	9.86E-01
J1125-5825	3.10E-03	6.00E-20	7.95E+34	4.40E+08	1.74E+00	6.45E-12	2.35E+33	3.29E+00	1.27E+00
J1125-6014	2.63E-03	2.08E-21	4.51E+33	1.00E+08	9.88E-01	3.09E-12	3.61E+32	1.72E+00	9.65E-01
J1137+7528	2.51E-03	3.20E-21	7.96E+33	9.07E+07	3.83E+00	6.01E-13	1.06E+33	1.72E+00	1.10E+00
J1142+0119	5.08E-03	1.50E-20	4.52E+33	2.79E+08	2.17E+00	6.44E-12	3.63E+33	3.88E+00	1.31E+00
J1151-6108	1.02E-01	1.03E-14	3.87E+35	1.03E+12	2.23E+00	1.03E-11	6.10E+33	2.44E+00	1.00E+00
J1207-5050	4.84E-03	5.88E-21	2.05E+33	1.74E+08	1.27E+00	4.79E-12	9.20E+32	1.73E+00	9.51E-01
J1221-0633	1.93E-03	1.09E-20	5.92E+34	1.46E+08	1.25E+00	5.82E-12	1.09E+33	3.14E+00	1.10E+00
J1227-4853	1.69E-03	1.07E-20	8.73E+34	1.52E+08	1.75E+00	1.90E-11	6.98E+33	5.54E+00	1.23E+00
J1231-1411	3.68E-03	7.18E-21	5.69E+33	2.83E+08	4.20E-01	1.01E-10	2.13E+33	2.54E+00	1.12E+00
J1253-5820	2.55E-01	2.11E-15	4.98E+33	7.42E+11	1.64E+00	4.26E-12	1.37E+33	6.75E-01	4.38E-01
J1301+0833	1.84E-03	6.89E-21	4.37E+34	1.41E+08	1.77E+00	7.69E-12	2.88E+33	2.48E+00	9.96E-01
J1302-3258	3.77E-03	4.90E-21	3.61E+33	1.59E+08	1.43E+00	1.09E-11	2.67E+33	2.41E+00	1.11E+00
J1311-3430	2.56E-03	2.05E-20	4.83E+34	2.34E+08	1.58E+00	6.06E-11	1.81E+34	5.10E+00	1.22E+00
J1312+0051	4.23E-03	8.70E-21	4.54E+33	2.72E+08	1.47E+00	1.46E-11	3.78E+33	1.93E+00	9.39E-01
J1341-6220	1.93E-01	2.53E-13	1.38E+36	7.08E+12	1.26E+01	2.23E-11	4.24E+35	1.69E+01	1.36E+00
J1357-6429	1.66E-01	3.54E-13	3.05E+36	7.76E+12	3.10E+00	2.95E-11	3.39E+34	1.91E+00	6.61E-01
J1400-1431	3.08E-03	3.62E-21	4.89E+33	1.51E+08	2.78E-01	6.42E-12	5.93E+31	1.97E+00	9.43E-01
J1402+1306	5.89E-03	1.35E-20	2.60E+33	2.85E+08	6.90E-01	1.60E-12	9.14E+31	1.18E+00	1.02E+00
J1410-6132	5.01E-02	3.18E-14	1.00E+37	1.28E+12	1.35E+01	2.28E-11	4.98E+35	2.23E+00	8.52E-01
J1418-6058	1.11E-01	1.71E-13	4.99E+36	4.40E+12	1.60E+00	2.97E-10	9.10E+34	3.62E+00	1.12E+00
J1420-6048	6.82E-02	8.24E-14	1.03E+37	2.40E+12	5.63E+00	1.29E-10	4.90E+35	3.21E+00	9.87E-01
J1431-4715	2.01E-03	1.12E-20	5.43E+34	1.70E+08	1.77E+00	4.65E-12	1.74E+33	2.15E+00	7.43E-01
J1446-4701	2.19E-03	9.63E-21	3.62E+34	1.48E+08	1.57E+00	7.69E-12	2.26E+33	3.87E+00	1.17E+00

Table A.1: *(Continued table from previous page)*

PSRJ	Period	$\dot{P}$	$\dot{E}$	B_{Star}	D3PC	Flux	Luminosity	e_{cut}	e_{10}
J1455-3330	7.99E-03	2.37E-20	1.83E+33	4.46E+08	6.84E-01	1.14E-12	6.36E+31	1.43E+00	8.54E-01
J1509-5850	8.89E-02	9.20E-15	5.17E+35	9.15E+11	3.37E+00	1.22E-10	1.66E+35	4.11E+00	1.17E+00
J1513-2550	2.12E-03	2.09E-20	8.68E+34	2.16E+08	3.96E+00	7.60E-12	1.43E+34	3.15E+00	1.04E+00
J1514-4946	3.59E-03	1.71E-20	1.46E+34	2.62E+08	9.08E-01	4.18E-11	4.13E+33	4.39E+00	1.29E+00
J1526-2744	2.49E-03	3.54E-21	9.05E+33	9.50E+07	1.32E+00	2.61E-12	5.43E+32	1.79E+00	1.02E+00
J1531-5610	8.42E-02	1.38E-14	9.12E+35	1.09E+12	2.84E+00	1.83E-11	1.76E+34	1.36E+00	7.70E-01
J1536-4948	3.08E-03	2.07E-20	2.79E+34	2.58E+08	9.78E-01	7.99E-11	9.14E+33	5.88E+00	1.44E+00
J1543-5149	2.06E-03	1.60E-20	7.22E+34	1.85E+08	1.15E+00	1.76E-11	2.78E+33	3.30E+00	9.77E-01
J1544+4937	2.16E-03	2.14E-21	8.40E+33	8.31E+07	2.99E+00	2.36E-12	2.53E+33	3.54E+00	1.22E+00
J1552+5437	2.43E-03	2.82E-21	7.79E+33	8.38E+07	2.64E+00	2.74E-12	2.28E+33	3.39E+00	1.16E+00
J1555-2908	1.79E-03	4.45E-20	3.08E+35	2.86E+08	5.10E+00	4.66E-12	1.45E+34	3.98E+00	9.67E-01
J1600-3053	3.60E-03	8.52E-21	7.21E+33	1.87E+08	1.92E+00	7.73E-12	3.42E+33	3.08E+00	1.23E+00
J1614-2230	3.15E-03	3.98E-21	5.03E+33	1.76E+08	7.00E-01	2.59E-11	1.52E+33	2.03E+00	1.13E+00
J1614-5048	2.32E-01	4.92E-13	1.56E+36	1.08E+13	5.15E+00	2.02E-11	6.40E+34	3.28E+00	1.04E+00
J1622-0315	3.85E-03	9.60E-21	6.64E+33	2.12E+08	1.23E+00	7.25E-12	1.31E+33	3.76E+00	1.17E+00
J1625-0021	2.83E-03	2.13E-20	3.70E+34	2.49E+08	9.51E-01	2.07E-11	2.24E+33	1.90E+00	9.93E-01
J1627+3219	2.18E-03	5.48E-21	2.08E+34	1.11E+08	4.47E+00	3.64E-12	8.71E+33	1.76E+00	1.02E+00
J1628-3205	3.21E-03	9.98E-21	1.19E+34	2.21E+08	1.19E+00	1.13E-11	1.92E+33	2.16E+00	9.10E-01
J1630+3734	3.32E-03	8.04E-21	8.67E+33	1.91E+08	1.19E+00	5.97E-12	1.01E+33	1.85E+00	9.76E-01
J1640+2224	3.16E-03	1.84E-21	2.31E+33	9.55E+07	1.52E+00	2.26E-12	6.21E+32	2.33E+00	1.08E+00
J1641+8049	2.01E-03	9.79E-21	4.68E+34	1.42E+08	3.04E+00	1.99E-12	2.19E+33	1.92E+00	9.11E-01
J1648-4611	1.65E-01	2.37E-14	2.09E+35	2.00E+12	4.47E+00	4.77E-11	1.14E+35	3.82E+00	1.28E+00
J1653-0158	1.97E-03	1.35E-21	6.96E+33	6.96E+07	7.40E-01	3.43E-11	2.25E+33	3.02E+00	9.87E-01
J1658-5324	2.44E-03	1.08E-20	2.93E+34	1.66E+08	8.80E-01	2.07E-11	1.92E+33	1.86E+00	7.91E-01
J1702-4128	1.82E-01	5.23E-14	3.42E+35	3.12E+12	3.97E+00	2.59E-11	4.88E+34	1.99E+00	8.40E-01
J1705-1906	2.99E-01	4.14E-15	6.11E+33	1.13E+12	7.47E-01	3.61E-12	2.41E+32	3.81E-01	4.45E-01
J1709-4429	1.03E-01	9.48E-14	3.48E+36	3.15E+12	2.60E+00	1.38E-09	1.11E+36	4.57E+00	1.29E+00
J1713+0747	4.57E-03	8.25E-21	3.41E+33	2.00E+08	1.31E+00	7.29E-12	1.50E+33	2.49E+00	1.10E+00

Table A.1: *(Continued table from previous page)*

PSRJ	Period	$\dot{P}$	$\dot{E}$	B_{Star}	D3PC	Flux	Luminosity	e_{cut}	e_{10}
J1718-3825	7.47E-02	1.32E-14	1.25E+36	1.00E+12	3.49E+00	1.04E-10	1.51E+35	3.40E+00	9.73E-01
J1730-2304	8.12E-03	1.47E-20	1.09E+33	4.10E+08	6.20E-01	8.58E-12	3.95E+32	1.10E+00	5.97E-01
J1730-3350	1.40E-01	8.41E-14	1.22E+36	3.47E+12	3.49E+00	4.36E-11	6.35E+34	4.03E+00	8.35E-01
J1731-4744	8.30E-01	1.64E-13	1.13E+34	1.18E+13	7.00E-01	3.93E-12	2.30E+32	1.70E-01	6.79E-02
J1732-3131	1.97E-01	2.80E-14	1.46E+35	2.38E+12	6.40E-01	1.79E-10	8.79E+33	2.23E+00	1.10E+00
J1732-5049	5.31E-03	1.14E-20	3.00E+33	2.78E+08	1.87E+00	5.64E-12	2.37E+33	2.89E+00	1.06E+00
J1739-3023	1.14E-01	1.14E-14	3.01E+35	1.16E+12	3.07E+00	2.12E-11	2.40E+34	1.53E+00	8.20E-01
J1740+1000	1.54E-01	2.13E-14	2.30E+35	1.83E+12	1.23E+00	3.60E-12	6.49E+32	5.08E-01	2.72E-01
J1741+1351	3.75E-03	2.80E-20	2.10E+34	3.41E+08	2.18E+00	3.57E-12	2.03E+33	2.34E+00	1.06E+00
J1741-2054	4.14E-01	1.70E-14	9.48E+33	2.68E+12	3.00E-01	1.19E-10	1.28E+33	9.58E-01	6.35E-01
J1744-1134	4.07E-03	7.11E-21	4.16E+33	1.93E+08	3.95E-01	3.71E-11	6.92E+32	1.43E+00	7.63E-01
J1745+1017	2.65E-03	2.05E-21	4.35E+33	8.27E+07	1.21E+00	7.60E-12	1.34E+33	2.33E+00	1.05E+00
J1747-2958	9.88E-02	6.11E-14	2.50E+36	2.49E+12	4.75E+00	1.59E-10	4.30E+35	2.90E+00	9.27E-01
J1747-4036	1.65E-03	1.30E-20	1.14E+35	1.50E+08	7.15E+00	1.34E-11	8.18E+34	2.89E+00	9.66E-01
J1801-2451	1.25E-01	8.95E-14	1.81E+36	3.38E+12	3.80E+00	3.19E-11	5.52E+34	5.62E+00	1.22E+00
J1803-6707	2.13E-03	1.76E-20	7.17E+34	2.01E+08	1.84E+00	4.78E-12	1.94E+33	6.61E+00	1.02E+00
J1805+0615	2.13E-03	1.86E-20	7.59E+34	2.23E+08	3.89E+00	5.27E-12	9.51E+33	2.26E+00	1.06E+00
J1809-2332	1.47E-01	3.44E-14	4.29E+35	2.27E+12	1.70E+00	4.25E-10	1.47E+35	3.67E+00	1.20E+00
J1810+1744	1.66E-03	4.24E-21	3.66E+34	8.87E+07	1.87E+00	2.33E-11	9.73E+33	3.75E+00	1.01E+00
J1811-2405	2.66E-03	1.29E-20	2.71E+34	1.91E+08	1.83E+00	1.38E-11	5.55E+33	9.26E+00	1.43E+00
J1816+4510	3.19E-03	4.37E-20	5.31E+34	3.75E+08	3.43E+00	1.06E-11	1.49E+34	3.21E+00	1.18E+00
J1823-3021A	5.44E-03	3.37E-18	8.27E+35	4.34E+09	7.60E+00	1.42E-11	9.82E+34	4.50E+00	1.28E+00
J1824-0621	3.23E-03	9.14E-21	1.07E+34	1.74E+08	3.53E+00	1.09E-11	1.63E+34	5.41E+00	1.02E+00
J1824+1014	4.07E-03	5.46E-21	3.21E+33	1.51E+08	2.90E+00	6.18E-12	6.23E+33	3.82E+00	1.25E+00
J1824-2452A	3.05E-03	1.61E-18	2.24E+36	2.25E+09	5.37E+00	2.24E-11	7.73E+34	2.82E+00	1.08E+00
J1828-1101	7.21E-02	1.48E-14	1.56E+36	1.05E+12	4.77E+00	4.77E-11	1.30E+35	5.47E+00	6.95E-01
J1831-0952	6.73E-02	8.31E-15	1.08E+36	7.57E+11	3.68E+00	5.44E-11	8.82E+34	8.46E-01	4.76E-01
J1833-1034	6.19E-02	2.02E-13	3.36E+37	3.58E+12	4.10E+00	8.91E-11	1.79E+35	5.54E+00	1.24E+00

Table A.1: *(Continued table from previous page)*

PSRJ	Period	$\dot{P}$	$\dot{E}$	B_{Star}	D3PC	Flux	Luminosity	e_{cut}	e_{10}
J1833-3840	1.87E-03	1.77E-20	1.08E+35	1.84E+08	4.65E+00	2.82E-12	7.29E+33	2.19E+00	9.47E-01
J1836+5925	1.73E-01	1.50E-15	1.14E+34	5.16E+11	5.30E-01	6.19E-10	2.08E+34	2.45E+00	1.02E+00
J1837-0604	9.63E-02	4.49E-14	1.98E+36	2.10E+12	4.78E+00	2.75E-11	7.52E+34	8.71E+00	1.37E+00
J1843-1113	1.85E-03	9.34E-21	5.82E+34	1.35E+08	1.26E+00	2.28E-11	4.33E+33	3.20E+00	8.17E-01
J1853-0004	1.01E-01	5.57E-15	2.11E+35	7.61E+11	5.34E+00	4.93E-12	1.68E+34	1.20E+00	1.05E+00
J1855-1436	3.59E-03	1.09E-20	9.29E+33	2.00E+08	5.13E+00	5.07E-12	1.59E+34	5.81E+00	1.42E+00
J1857+0143	1.40E-01	3.10E-14	4.49E+35	2.11E+12	4.57E+00	1.17E-11	2.92E+34	1.15E+00	9.28E-01
J1858-2216	2.38E-03	3.50E-21	1.03E+34	9.71E+07	9.21E-01	1.14E-11	1.16E+33	1.90E+00	1.02E+00
J1901-0125	2.79E-03	3.58E-20	6.48E+34	3.20E+08	2.36E+00	1.95E-11	1.30E+34	3.61E+00	1.11E+00
J1902-5105	1.74E-03	8.58E-21	6.43E+34	1.27E+08	1.65E+00	2.35E-11	7.62E+33	3.77E+00	1.09E+00
J1903-7051	3.60E-03	7.92E-21	6.70E+33	1.96E+08	9.30E-01	5.28E-12	5.46E+32	2.47E+00	1.14E+00
J1907+0602	1.07E-01	8.65E-14	2.81E+36	3.07E+12	2.58E+00	2.97E-10	2.36E+35	3.72E+00	1.15E+00
J1908+2105	2.56E-03	1.31E-20	3.09E+34	1.90E+08	2.60E+00	4.88E-12	3.95E+33	5.14E+00	1.32E+00
J1913+0904	1.63E-01	1.76E-14	1.60E+35	1.72E+12	3.00E+00	1.98E-11	2.12E+34	2.21E+00	1.02E+00
J1921+0137	2.50E-03	1.90E-20	4.81E+34	2.19E+08	5.09E+00	1.08E-11	3.35E+34	4.31E+00	1.20E+00
J1921+1929	2.65E-03	3.65E-20	7.74E+34	3.22E+08	2.43E+00	3.49E-12	2.48E+33	2.62E+00	1.16E+00
J1925+1720	7.57E-02	1.05E-14	9.54E+35	9.00E+11	5.05E+00	9.53E-12	2.90E+34	1.82E+00	8.75E-01
J1932+2220	1.44E-01	5.70E-14	7.46E+35	2.90E+12	1.09E+01	5.16E-12	7.34E+34	2.56E+00	9.66E-01
J1935+2025	8.00E-02	6.04E-14	4.64E+36	2.23E+12	4.60E+00	2.17E-11	5.49E+34	1.77E+00	7.09E-01
J1939+2134	1.56E-03	1.05E-19	1.10E+36	4.10E+08	3.07E+00	2.07E-11	2.33E+34	3.21E+00	9.76E-01
J1946-5403	2.71E-03	2.69E-21	5.33E+33	8.64E+07	1.15E+00	9.83E-12	1.56E+33	1.30E+00	8.43E-01
J1952+3252	3.95E-02	5.83E-15	3.72E+36	4.86E+11	3.00E+00	1.48E-10	1.59E+35	3.74E+00	1.13E+00
J1959+2048	1.61E-03	1.24E-20	1.17E+35	1.67E+08	1.27E+00	1.57E-11	3.02E+33	2.06E+00	9.13E-01
J2006+0148	2.16E-03	3.29E-21	1.28E+34	8.53E+07	2.44E+00	3.03E-12	2.15E+33	4.17E+00	1.37E+00
J2006+3102	1.64E-01	2.49E-14	2.24E+35	2.04E+12	6.04E+00	1.06E-11	4.63E+34	3.08E+00	1.10E+00
J2017+0603	2.90E-03	8.52E-21	1.38E+34	1.57E+08	1.40E+00	3.56E-11	8.34E+33	3.85E+00	1.27E+00
J2017-1614	2.31E-03	2.41E-21	7.67E+33	7.54E+07	1.44E+00	6.47E-12	1.61E+33	4.14E+00	1.22E+00
J2021+3651	1.04E-01	9.48E-14	3.35E+36	3.17E+12	1.80E+00	4.92E-10	1.91E+35	3.25E+00	1.11E+00

Table A.1: *(Continued table from previous page)*

PSRJ	Period	$\dot{P}$	$\dot{E}$	B_{Star}	D3PC	Flux	Luminosity	e_{cut}	e_{10}
J2021+4026	2.65E-01	5.48E-14	1.16E+35	3.86E+12	1.50E+00	8.01E-10	2.16E+35	2.68E+00	9.45E-01
J2022+3842	4.86E-02	8.62E-14	2.97E+37	2.07E+12	1.00E+01	2.65E-11	3.17E+35	2.51E+00	6.94E-01
J2030+3641	2.00E-01	6.51E-15	3.20E+34	1.15E+12	3.00E+00	4.23E-11	4.55E+34	1.95E+00	1.00E+00
J2030+4415	2.27E-01	5.05E-15	1.70E+34	1.08E+12	5.00E-01	4.43E-11	1.32E+33	1.56E+00	8.35E-01
J2032+4127	1.43E-01	1.16E-14	1.56E+35	1.31E+12	1.76E+00	1.42E-10	5.28E+34	4.03E+00	1.34E+00
J2039-3616	3.27E-03	6.34E-21	7.16E+33	1.68E+08	1.70E+00	3.82E-12	1.33E+33	2.41E+00	9.67E-01
J2039-5617	2.65E-03	1.20E-20	2.54E+34	1.96E+08	1.68E+00	1.54E-11	5.21E+33	4.46E+00	1.16E+00
J2042+0246	4.53E-03	1.41E-20	5.97E+33	2.56E+08	6.40E-01	5.83E-12	2.86E+32	1.00E+00	6.36E-01
J2043+1711	2.38E-03	4.80E-21	1.41E+34	1.18E+08	1.39E+00	2.85E-11	6.57E+33	3.87E+00	1.23E+00
J2043+2740	9.61E-02	1.24E-15	5.50E+34	3.49E+11	1.48E+00	9.03E-12	2.37E+33	1.38E+00	7.11E-01
J2047+1053	4.29E-03	1.37E-20	6.83E+33	3.04E+08	2.79E+00	4.26E-12	3.98E+33	6.18E+00	1.47E+00
J2051-0827	4.51E-03	1.28E-20	5.50E+33	2.42E+08	1.47E+00	2.50E-12	6.46E+32	1.80E+00	1.03E+00
J2052+1219	1.99E-03	2.09E-21	1.05E+34	1.17E+08	5.57E+00	4.57E-12	1.70E+34	7.45E+00	1.31E+00
J2115+5448	2.61E-03	2.93E-20	6.50E+34	3.05E+08	3.11E+00	7.02E-12	8.10E+33	2.41E+00	1.18E+00
J2116+1345	2.22E-03	2.64E-21	9.55E+33	7.75E+07	2.73E+00	2.90E-12	2.59E+33	5.83E+00	1.02E+00
J2124-3358	4.93E-03	7.57E-21	2.49E+33	3.22E+08	4.10E-01	3.88E-11	7.80E+32	1.78E+00	9.71E-01
J2129-0429	7.61E-03	2.30E-19	2.06E+34	1.36E+09	1.83E+00	6.81E-12	2.73E+33	2.71E+00	1.08E+00
J2208+4056	6.37E-01	5.28E-15	8.07E+32	1.86E+12	7.54E-01	4.63E-12	3.15E+32	4.52E-01	2.39E-01
J2214+3000	3.12E-03	1.33E-20	1.72E+34	2.19E+08	6.00E-01	3.26E-11	1.41E+33	2.07E+00	9.92E-01
J2215+5135	2.61E-03	2.38E-20	5.27E+34	2.50E+08	2.66E+00	1.80E-11	1.53E+34	4.58E+00	1.28E+00
J2229+6114	5.17E-02	7.53E-14	2.16E+37	1.99E+12	3.00E+00	2.40E-10	2.59E+35	4.93E+00	1.22E+00
J2234+0944	3.63E-03	1.34E-20	1.11E+34	2.70E+08	7.04E-01	1.00E-11	5.95E+32	3.01E+00	1.20E+00
J2240+5832	1.40E-01	1.53E-14	2.20E+35	1.48E+12	7.28E+00	9.82E-12	6.22E+34	4.07E+00	1.16E+00
J2241-5236	2.19E-03	6.99E-21	2.63E+34	1.40E+08	1.04E+00	2.50E-11	3.25E+33	1.93E+00	9.83E-01
J2256-1024	2.29E-03	1.16E-20	3.83E+34	1.63E+08	2.08E+00	8.18E-12	4.25E+33	2.58E+00	1.03E+00
J2302+4442	5.19E-03	1.34E-20	3.77E+33	2.66E+08	8.63E-01	3.90E-11	3.47E+33	3.02E+00	1.16E+00
J2310-0555	2.61E-03	4.96E-21	1.10E+34	1.15E+08	1.56E+00	5.60E-12	1.62E+33	2.04E+00	9.97E-01
J2317+1439	3.45E-03	3.00E-21	2.89E+33	9.27E+07	1.70E+00	6.17E-13	2.13E+32	2.68E-01	5.47E-01

Table A.1: *(Continued table from previous page)*

PSRJ	Period	$\dot{P}$	$\dot{E}$	B_{Star}	D3PC	Flux	Luminosity	e_{cut}	e_{10}
J2339-0533	2.88E-03	1.36E-20	2.25E+34	2.04E+08	1.30E+00	2.92E-11	5.90E+33	4.03E+00	1.25E+00

Table A.2: 62 pulsars with unknown distance values and their relevant parameters used in this study.

PSRJ	Period	$\dot{P}$	$\dot{E}$	B_{Star}	D3PC	Flux	Luminosity	e_{cut}	e_{10}
J0357+3205	4.44E-01	1.31E-14	5.90E+33	2.44E+12	7.12E+00	6.01E-11	3.65E+35	1.19E+00	6.73E-01
J0359+5414	7.94E-02	1.67E-14	1.32E+36	1.17E+12	9.22E+00	1.98E-11	2.02E+35	2.37E+00	9.88E-01
J0554+3107	4.65E-01	1.43E-13	5.60E+34	8.24E+12	9.03E+00	1.87E-11	1.82E+35	1.58E+00	8.34E-01
J0622+3749	3.33E-01	2.54E-14	2.71E+34	2.94E+12	7.95E+00	1.77E-11	1.34E+35	8.28E-01	5.61E-01
J0633+0632	2.97E-01	7.96E-14	1.19E+35	4.92E+12	9.66E+00	9.56E-11	1.07E+36	3.05E+00	1.11E+00
J0734-1559	1.55E-01	1.25E-14	1.32E+35	1.41E+12	9.65E+00	4.57E-11	5.10E+35	3.69E+00	1.02E+00
J0744-2525	9.20E-02	9.31E-16	4.72E+34	2.96E+11	1.06E+01	1.73E-11	2.33E+35	2.38E+00	9.97E-01
J0802-5613	2.74E-01	2.78E-15	5.33E+33	8.83E+11	1.10E+01	6.59E-12	9.60E+34	1.34E+00	7.99E-01
J1023-5746	1.11E-01	3.80E-13	1.08E+37	6.59E+12	1.19E+01	1.46E-10	2.46E+36	3.42E+00	9.88E-01
J1044-5737	1.39E-01	5.46E-14	8.02E+35	2.79E+12	1.12E+01	1.14E-10	1.70E+36	3.43E+00	9.96E-01
J1057-5851	6.20E-01	1.01E-13	1.66E+34	7.99E+12	1.16E+01	1.32E-11	2.12E+35	1.03E+00	7.07E-01
J1105-6037	1.95E-01	2.18E-14	1.16E+35	2.09E+12	1.27E+01	3.07E-11	5.90E+35	3.19E+00	1.06E+00
J1111-6039	1.07E-01	1.95E-13	6.35E+36	4.62E+12	1.28E+01	5.91E-11	1.16E+36	4.26E+00	1.48E+00
J1135-6055	1.14E-01	7.82E-14	2.06E+36	3.03E+12	1.35E+01	4.58E-11	1.00E+36	3.81E+00	1.10E+00
J1139-6247	1.20E-01	4.06E-15	9.17E+34	7.08E+11	1.44E+01	1.92E-11	4.77E+35	6.15E+00	1.41E+00
J1203-6242	1.01E-01	4.45E-14	1.73E+36	2.14E+12	1.50E+01	3.74E-11	1.01E+36	3.97E+00	1.14E+00
J1208-6238	4.41E-01	3.31E-12	1.53E+36	3.86E+13	1.51E+01	3.73E-11	1.02E+36	5.97E+00	1.30E+00
J1231-5113	2.07E-01	1.15E-16	5.16E+32	1.56E+11	1.02E+01	1.07E-11	1.33E+35	8.95E-01	5.34E-01
J1231-6511	2.48E-01	2.82E-14	7.34E+34	2.67E+12	1.70E+01	1.21E-11	4.20E+35	1.94E+00	8.58E-01
J1335-5656	3.24E-03	1.26E-20	1.46E+34	2.04E+08	1.50E+01	8.22E-12	2.23E+35	3.82E+00	1.24E+00
J1350-6225	1.38E-01	8.88E-15	1.33E+35	1.12E+12	1.74E+01	3.60E-11	1.30E+36	3.49E+00	1.20E+00
J1358-6025	6.05E-02	3.00E-15	5.35E+35	4.32E+11	1.66E+01	3.17E-11	1.05E+36	3.84E+00	1.06E+00
J1413-6205	1.10E-01	2.74E-14	8.18E+35	1.75E+12	1.80E+01	1.78E-10	6.87E+36	3.85E+00	1.28E+00
J1422-6138	3.41E-01	9.68E-14	9.64E+34	5.81E+12	1.82E+01	5.35E-11	2.11E+36	3.33E+00	1.35E+00
J1429-5911	1.16E-01	2.39E-14	6.06E+35	1.68E+12	1.74E+01	1.13E-10	4.10E+36	3.60E+00	9.91E-01
J1447-5757	1.59E-01	1.18E-14	1.17E+35	1.39E+12	1.82E+01	2.34E-11	9.32E+35	1.76E+00	6.75E-01

Table A.2: *(Continued table from previous page)*

PSRJ	Period	$\dot{P}$	$\dot{E}$	B_{Star}	D3PC	Flux	Luminosity	e_{cut}	e_{10}
J1459-6053	1.03E-01	2.53E-14	9.08E+35	1.63E+12	1.97E+01	1.23E-10	5.69E+36	3.84E+00	9.69E-01
J1522-5735	2.04E-01	6.25E-14	2.89E+35	3.61E+12	1.93E+01	7.59E-11	3.38E+36	2.79E+00	9.69E-01
J1528-5838	3.56E-01	2.48E-14	2.17E+34	3.00E+12	2.05E+01	1.81E-11	9.07E+35	2.38E+00	1.04E+00
J1615-5137	1.79E-01	1.06E-14	7.28E+34	1.40E+12	1.86E+01	3.34E-11	1.38E+36	2.29E+00	1.15E+00
J1620-4927	1.72E-01	1.05E-14	8.15E+34	1.36E+12	1.84E+01	1.29E-10	5.23E+36	4.15E+00	1.26E+00
J1623-5005	8.51E-02	4.16E-15	2.67E+35	6.02E+11	1.84E+01	6.11E-11	2.48E+36	3.74E+00	1.48E+00
J1624-4041	1.68E-01	4.72E-15	3.94E+34	9.01E+11	1.81E+01	2.74E-11	1.08E+36	2.45E+00	9.82E-01
J1641-5317	1.75E-01	3.70E-15	2.72E+34	8.15E+11	2.23E+01	1.48E-11	8.82E+35	1.85E+00	8.56E-01
J1649-3012	3.42E-03	1.29E-20	1.27E+34	2.13E+08	1.58E+01	9.04E-12	2.71E+35	2.59E+00	1.07E+00
J1650-4601	1.27E-01	1.51E-14	2.91E+35	1.40E+12	2.26E+01	5.61E-11	3.43E+36	2.96E+00	1.06E+00
J1714-3830	8.41E-02	7.03E-14	4.66E+36	2.46E+12	2.05E+01	9.12E-11	4.59E+36	5.11E+00	1.51E+00
J1736-3422	3.47E-01	6.51E-14	6.14E+34	4.81E+12	2.18E+01	1.75E-11	9.90E+35	2.85E+00	1.11E+00
J1742-3321	1.43E-01	1.27E-15	1.71E+34	4.32E+11	2.21E+01	1.45E-11	8.50E+35	2.01E+00	9.95E-01
J1744-7619	4.69E-03	9.67E-21	3.71E+33	2.16E+08	1.50E+00	1.97E-11	5.31E+33	1.77E+00	9.50E-01
J1746-3239	2.00E-01	6.56E-15	3.26E+34	1.16E+12	2.22E+01	5.13E-11	3.02E+36	2.45E+00	1.00E+00
J1803-2149	1.06E-01	1.95E-14	6.40E+35	1.46E+12	2.18E+01	8.92E-11	5.09E+36	4.33E+00	1.31E+00
J1813-1246	4.81E-02	1.76E-14	6.24E+36	9.30E+11	2.25E+01	2.48E-10	1.50E+37	3.20E+00	9.15E-01
J1817-1742	1.50E-01	2.06E-14	2.42E+35	1.78E+12	2.20E+01	2.85E-11	1.65E+36	4.83E+00	1.22E+00
J1826-1256	1.10E-01	1.21E-13	3.57E+36	3.70E+12	1.90E+01	4.13E-10	1.80E+37	3.62E+00	1.06E+00
J1827-0849	2.24E-03	1.10E-20	3.84E+34	1.59E+08	2.23E+01	2.95E-11	1.76E+36	1.05E+01	1.41E+00
J1827-1446	4.99E-01	4.53E-14	1.44E+34	4.81E+12	2.20E+01	1.94E-11	1.13E+36	9.31E-01	8.74E-01
J1838-0537	1.46E-01	4.51E-13	5.75E+36	8.20E+12	1.82E+01	1.20E-10	4.74E+36	3.86E+00	1.30E+00
J1844-0346	1.13E-01	1.55E-13	4.25E+36	4.23E+12	1.74E+01	4.59E-11	1.66E+36	2.23E+00	1.01E+00
J1846+0919	2.26E-01	9.93E-15	3.42E+34	1.51E+12	2.17E+01	3.57E-11	2.01E+36	2.42E+00	1.05E+00
J1906+0722	1.12E-01	3.59E-14	1.02E+36	2.02E+12	1.89E+01	8.59E-11	3.66E+36	4.48E+00	1.10E+00
J1932+1916	2.08E-01	9.32E-14	4.07E+35	4.46E+12	1.77E+01	6.55E-11	2.46E+36	2.60E+00	9.01E-01
J1954+2836	9.27E-02	2.12E-14	1.05E+36	1.42E+12	1.64E+01	1.07E-10	3.45E+36	3.75E+00	1.20E+00
J1957+5033	3.75E-01	7.08E-15	5.31E+33	1.65E+12	1.47E+01	2.62E-11	6.73E+35	1.25E+00	6.40E-01

Table A.2: *(Continued table from previous page)*

PSRJ	Period	$\dot{P}$	$\dot{E}$	B_{Star}	D3PC	Flux	Luminosity	e_{cut}	e_{10}
J1958+2846	2.90E-01	2.12E-13	3.41E+35	7.93E+12	1.61E+01	1.06E-10	3.28E+36	2.79E+00	1.07E+00
J2017+3625	1.67E-01	1.36E-15	1.16E+34	4.82E+11	1.50E+01	7.52E-11	2.01E+36	2.17E+00	8.85E-01
J2028+3332	1.77E-01	4.86E-15	3.48E+34	9.37E+11	1.45E+01	5.71E-11	1.43E+36	1.65E+00	9.57E-01
J2034+3632	3.65E-03	1.73E-21	1.41E+33	8.05E+07	1.41E+01	1.24E-11	2.96E+35	1.91E+00	1.13E+00
J2055+2539	3.20E-01	4.10E-15	4.96E+33	1.16E+12	1.09E+01	5.32E-11	7.50E+35	1.49E+00	8.20E-01
J2111+4606	1.58E-01	1.63E-13	1.63E+36	5.13E+12	1.28E+01	4.89E-11	9.65E+35	5.02E+00	1.26E+00
J2139+4716	2.83E-01	1.78E-15	3.11E+33	7.18E+11	1.20E+01	2.70E-11	4.65E+35	1.10E+00	7.16E-01
J2238+5903	1.63E-01	9.69E-14	8.87E+35	4.02E+12	1.14E+01	6.64E-11	1.02E+36	3.69E+00	1.05E+00